NEUROSCIENCE

Distributed burst firing mediates optimized cortical encoding of natural self-motion

Jerome Carriot[1], Isabelle Mackrous[1], Kathleen E. Cullen[2,3,4,5], Maurice J. Chacron[1]*

Accurate perception of self-motion requires that vestibular input be transformed into neural representations suitable for integrating multisensory cues to guide action. Here, we demonstrate that vestibular cortical neurons represent the self-motion stimuli encountered during everyday activities in a fundamentally different manner than the artificial self-motion stimuli typically used. Using stimuli whose waveforms reproduce the head dynamics encountered in natural behavior, we found that neural activity no longer tracked stimulus velocity through graded firing-rate changes, as observed during artificial sinusoidal stimulation, but instead reliably encoded distinct motion features through burst firing. At the population level, these bursts formed a distributed code that enhanced information transmission by reducing redundancy. This transformation emerged only during natural stimulation and was absent in the vestibular thalamus. Together, our results demonstrate that the vestibular cortex constructs a distributed, feature-based representation of natural self-motion, fundamentally reshaping our understanding of how cortical circuits encode vestibular signals to mediate perception.

INTRODUCTION

Self-motion is sensed by the vestibular system, contributing to reflexes, spatial perception, and motor coordination during everyday life [reviewed in (*1*)]. Vestibular sensors detect head movement information, transmitting this information via afferents to the vestibular nuclei (VN). Vestibular-only neurons within the VN project to neurons in the thalamic ventral posteriolateral area (VPL) (*2*, *3*). The VPL projects directly to multiple cortical areas that are involved in self-motion processing and perception, including the parietoinsular vestibular cortex (PIVC), the ventral intraparietal cortex (VIP), area 2v of the intraparietal sulcus, and area 3a in the sulcus centralis (*4*–*7*). Area PIVC further receives both visual inputs from the medial temporal (MT) via the dorsal medial superior temporal (MSTd) cortex (*6*, *8*–*10*), projects to the VIP (*7*), and is furthermore strongly interconnected with somatosensory cortex areas 3a and 2v (*8*). Notably, PIVC is thought to play a central role in mediating self-motion perception: Stimulation of this area evokes vestibular sensations (*11*), whereas lesions instead impair orientation perception (*12*, *13*).

The common wisdom is that neurons within ascending vestibular pathways exclusively transmit information through changes in firing rate that are linearly related to the self-motion stimulus [see (*1*, *14*) for review]. However, the self-motion stimuli experienced during everyday behavior fundamentally differ from the artificial sinusoidal stimuli typically used in neurophysiological studies (*15*, *16*). Subcortical vestibular neurons in both VN and VPL demonstrate strong nonlinearities (*17*) and respond with markedly different dynamics to natural versus artificial self-motion (*18*–*21*) [see (*22*, *23*) for review]. This raises a fundamental question: Do cortical representations of vestibular input driven by artificial stimuli accurately generalize to natural self-motion? In particular, subcortical neurons respond to naturalistic stimuli using precise spike timing (*24*), thereby suggesting that specific action potential patterns carry information. Perhaps one of the most commonly encountered action potential pattern is burst firing (i.e., the tendency of neurons to fire packets of action potentials followed by quiescence) (*25*). This mode of activity is observed across diverse brain regions, including the hippocampus (*26*–*28*) and avian forebrain (*29*, *30*) [see (*25*, *31*, *32*) for review], and arises from well-characterized somato-dendritic interactions (*27*, *33*). Despite its ubiquity and mechanistic understanding, whether burst firing contributes to the encoding of self-motion within cortical pathways remains unknown.

Accordingly, here we investigated how neurons in the macaque PIVC encode both natural and artificial self-motion. Consistent with prior results, PIVC neurons encoded the detailed time course of sinusoidal (artificial) motion. In notable contrast, during natural self-motion, cortical neurons adopted a fundamentally different coding strategy, reliably signaling distinct stimulus features through burst firing. This nonlinear transformation emerged within the cortex as the response of vestibular thalamic neurons in VPL continued to follow stimulus dynamics under both conditions. Computational modeling further revealed that this thalamic-cortical transformation emerges under richer self-motion stimulus statistics. Our modeling also predicted that PIVC representations of natural stimuli are distributed, requiring pooling across neurons to recover stimulus dynamics—a prediction that was confirmed experimentally. Together, these findings demonstrate that PIVC does not passively relay vestibular input to higher brain areas with little to no transformation. Rather, they identify the vestibular cortex as an essential site of thalamic-cortical transformation that recodes vestibular signals into distributed, feature-based population representations where each neuron signals a specific stimulus feature (e.g., upstroke) via burst firing thereby supporting perception of natural self-motion.

RESULTS

The goal of this study was to investigate how neural populations within PIVC that receive direct input from VPL neurons encode natural self-motion (Fig. 1A). To address this question, we delivered passive motion to head-fixed rhesus macaques (*Macaca mulatta*) that were seated on a turntable (Fig. 1B, left) during rotations along the yaw axis. The time course of these rotations was either sinusoidal

[1]Department of Physiology, McGill University, Montreal, Canada. [2]Department of Biomedical Engineering, Johns Hopkins University, Baltimore, MD, USA. [3]Department of Otolaryngology-Head and Neck Surgery, Johns Hopkins University School of Medicine, Baltimore, MD, USA. [4]Department of Neuroscience, Johns Hopkins University School of Medicine, Baltimore, MD, USA. [5]Kavli Neuroscience Discovery Institute, Johns Hopkins University, Baltimore, MD, USA.
*Corresponding author. Email: maurice.chacron@mcgill.ca

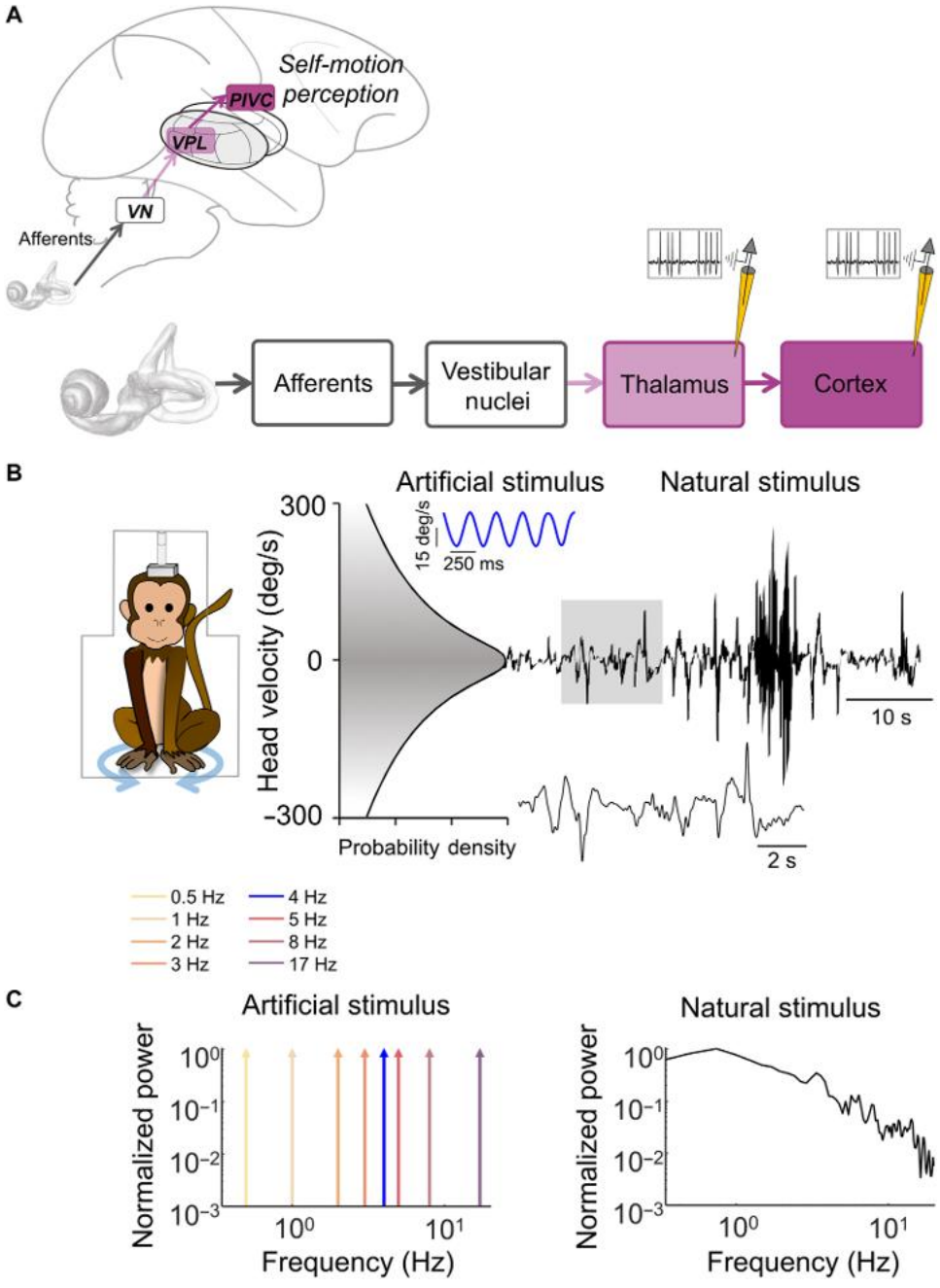

Fig. 1. Experimental setup and stimuli used in this study. (**A**) Schematic of the brain showing ascending vestibular pathways. Vestibular afferents transmit head motion information to neurons within the VN, which, in turn, project to the VPL area of the thalamus as well as the PIVC that mediate self-motion perception. We recorded from neurons within the VPL and PIVC in this study. (**B**) Left: The monkey was seated in a primate chair that was mounted on a motion platform. Right: Stimuli consisted of rotations along the YAW axis whose time course was either sinusoidal (i.e., artificial and middle) or closely resembled that experienced during natural behaviors (i.e., natural and right). (**C**) Left: Sinusoids contain power only at the stimulus frequency, which is represented by the different colored arrows. Right: Natural stimuli instead display power for a spectrum of frequencies.

(i.e., artificial; Fig. 1B, middle, yellow curve) or mimicked that recorded while the animal performed natural behaviors such as walking or jumping (i.e., natural; Fig. 1B, right, black curve; see Materials and Methods). We used sinusoidal stimuli with an amplitude of 15°/s at frequencies 0.5, 1, 2, 3, 4, 5, 8, and 17 Hz, which span the natural range. Natural stimuli consisted of 60-s snippets of horizontal angular velocity from naturally behaving rhesus macaques (*18*, *19*), played back through the motion platform. These natural stimuli reached much higher amplitudes (~200°/s; Fig. 1B) and contained a spectrum of frequencies (Fig. 1C, right). Our dataset consisted of well-isolated single neurons from three animals from areas VPL and PIVC (VPL: $N = 27$; PIVC: $N = 37$; see Materials and Methods). All neurons that

were sensitive to sinusoidal vestibular stimulation and whose isolation met or exceeded our criteria as well as could be maintained during stimulation were included in our dataset.

Vestibular cortical neurons encode the detailed time course of artificial but not natural self-motion

We recorded the activities of vestibular cortical neurons within PIVC during artificial sinusoidal and natural stimulation (Fig. 2A). The firing rate and unit activity (UA) of an example neuron during artificial and natural stimulation are shown in Fig. 2 (B and C), respectively. During artificial stimulation, this neuron's activity was modulated, such that the firing rate followed the stimulus' detailed time course (Fig. 2B). We further applied standard models based on linear systems characterization (*9*, *34*) and found that the predicted firing rates matched those observed experimentally for all frequencies (Fig. 2B, compare shaded gray with dashed lines). In contrast,

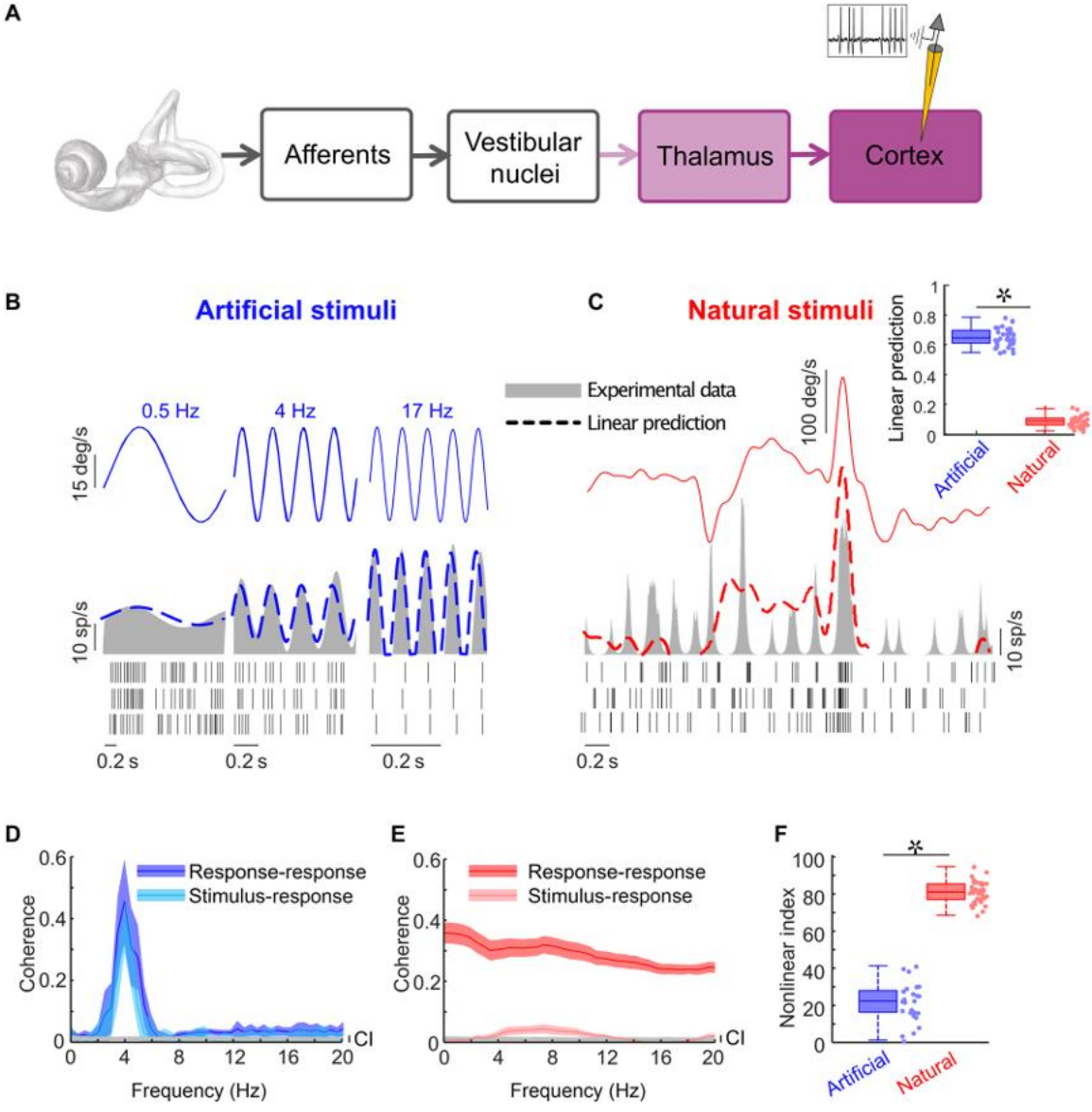

Fig. 2. Vestibular cortical neurons encode the detailed time course of artificial but not natural stimuli. (**A**) Schematic showing ascending vestibular pathways; recordings were made from vestibular cortical neurons. (**B**) Angular velocity (top), firing rate (middle), and UA (bottom) from an example vestibular cortical neuron during artificial stimulation. Shown are stimulus waveforms (top), firing rates (middle), and UAs (bottom) for three frequencies (left: 0.5 Hz; middle: 4 Hz; right: 17 Hz). The firing rate followed the detailed time course of the stimulus and was well predicted by linear models (dashed line). (**C**) Same as (B), but during natural stimulation. The firing rate did not follow the stimulus' detailed time course and was not well predicted by linear models. Inset: The goodness of fit was significantly higher during artificial stimulation (Wilcoxon signed-rank, $Z = 5.3$, $P \approx 5.71 \times 10^{-8}$). (**D**) Plots showing the population-averaged stimulus-response (light blue) and square root of response-response coherence (dark blue) curves as a function of frequency during artificial 4-Hz sinusoidal stimulation. CI, confidence interval. (**E**) Plots showing the population-averaged stimulus-response (light red) and square root of response-response coherence (dark red) curves as a function of frequency during natural stimulation. (**F**) Whisker-box plots showing the nonlinearity index during artificial (blue) and natural (red) stimulation. Values during natural stimulation were significantly higher (Wilcoxon signed-rank test, $Z = -4.46$, $P \approx 8.3 \times 10^{-6}$).

the response of this same neuron to natural stimulation did not follow the stimulus at all (Fig. 2C, compare dashed red and gray traces). Linear models performed poorly at predicting the neural response, which was not related to the stimulus in any obvious manner.

We hypothesized that the inability of vestibular cortical neurons to follow the detailed stimulus time course during natural stimulation was due to nonlinear encoding. To test this, we compared the stimulus-response and response-response coherence curves for each neuron (see Materials and Methods). If a neuron's response is linearly related to the stimulus, these two curves should overlap; any difference thus indicates a response nonlinearity (*35*–*37*). During artificial stimulation, both curves exhibited high coherence and closely overlapped (Fig. 2D). In contrast, during natural stimulation, the stimulus-response coherence curve was near zero (Fig. 2E), as expected because linear models could not accurately predict the observed responses (Fig. 2C). Notably, the response-response coherence curve was systematically higher than the stimulus-response coherence (Fig. 2E), revealing strong nonlinearities in cortical activity. The nonzero response-response coherence further confirms that cortical neurons did respond to the natural self-motion stimulus. We then quantified response nonlinearity by computing a nonlinearity index (see Materials and Methods) and found much higher values during natural stimulation (Fig. 2F; Wilcoxon signed-rank test, $Z = -4.46$, $P \approx 8.3 \times 10^{-6}$), thereby confirming our hypothesis that vestibular cortical neurons exhibit markedly nonlinear responses under natural stimulation.

To compare with previous results, we used linear systems identification techniques to quantify the gain and phase as a function of frequency during both natural and artificial stimulation (see Materials and Methods). Response gains and phases obtained during artificial stimulation were similar to those obtained previously (*13*, *34*). Vestibular cortical neurons displayed high-pass tuning with response gains that increased as a function of frequency (fig. S1, top left). In contrast, during natural stimulation, response gain was low irrespective of frequency (fig. S1, top right), which is expected because responses were strongly nonlinear (Fig. 2E). As a result, linear models performed much better at predicting responses to artificial stimulation (Fig. 2C, inset), which is expected as neural responses were then more linearly related to the stimulus (Fig. 2D).

Vestibular thalamic neurons encode the detailed time course of both artificial and natural self-motion

Perhaps the simplest explanation for the differential responses of vestibular cortical neurons to natural and artificial stimulation is that these are simply inherited from vestibular thalamic neurons. To test this prediction, we performed recordings from vestibular thalamic neurons within VPL during artificial and natural stimulation (Fig. 3A). Overall, we found that vestibular thalamic neuron activity followed the stimulus' detailed time course during both artificial (Fig. 3B) and natural (Fig. 3C) stimulation consistent with the previous literature (*38*, *39*). Moreover, the stimulus-response and response-response coherence curves closely matched during both artificial (Fig. 3D) and natural stimulation (Fig. 3E), indicating that neuronal responses were linearly related to the stimulus under both conditions.

Nonlinearity index values were much more similar to one another than for vestibular cortical neurons (compare Fig. 3F with Fig. 2F). Quantification of results using linear systems identification techniques further revealed important differences between gain and phase during artificial and natural stimulation (fig. S1, bottom). Such differences are due to response nonlinearities such as contrast gain control that have been well-characterized previously (*20*, *40*–*42*). However, such nonlinearities are qualitatively different than those observed for vestibular cortical neurons above as, in each case, the neural activity is well predicted by (albeit different) linear models (Fig. 3, B and C). As such, we conclude that the differential responses of vestibular cortical neurons during artificial and natural stimulation are not inherited from afferent thalamic input.

Single vestibular cortical neurons transmit little information about the stimulus' detailed time course during natural stimulation

We next quantified the information transmitted by the spiking activities of vestibular cortical and thalamic neurons during artificial and natural stimulation. To do so, we quantified the performance of an optimal linear decoder at reconstructing the stimulus' detailed time course from the spiking activity (*43*, *44*). Specifically, the reconstructed stimulus waveform is obtained by convolving the spike train with a kernel that is chosen to minimize the mean square error between the actual and reconstructed stimulus waveforms (Fig. 4, A and B; see Materials and Methods). Overall, for cortical neurons, we predicted a much better match between the actual and reconstructed stimulus waveforms during artificial stimulation. For thalamic neurons, we instead predicted a good match during both artificial and natural stimulation. Consistent with our predictions, for cortical neurons, the actual and reconstructed waveforms closely resembled one another during artificial 4-Hz stimulation (Fig. 4A, compare blue and orange waveforms) but instead strongly differed during natural stimulation (Fig. 4B, compare red and orange waveforms). Similar results were obtained for all sinewave frequencies (fig. S2). For thalamic neurons, the waveforms closely resembled one another during both artificial (Fig. 4C, compare blue and orange waveforms) and natural (Fig. 4D, compare red and orange waveforms) stimulation.

We quantified the quality of the reconstruction by computing the coding fraction, which ranges between 0 and 1 and represents the fraction of the stimulus that is correctly reconstructed (see Materials and Methods). We also computed the mutual information rate between the original and reconstructed stimulus waveforms (see Materials and Methods). Overall, during artificial stimulation, coding fraction and mutual information values were more similar between vestibular cortical and thalamic neurons (Mann-Whitney U tests; coding fraction: $U = 805$; $P \approx 3.7 \times 10^{-7}$; mutual information: $U = 450$; $P \approx 0.86$; Fig. 4E). In contrast, during natural stimulation, both coding fraction and mutual information values were much lower for vestibular cortical neurons (Mann-Whitney U tests; coding fraction: $U = 875$; $P \approx 5.7 \times 10^{-11}$; mutual information: $U = 875$; $P \approx 6.2 \times 10^{-11}$; Fig. 4F). Furthermore, for cortical neurons, coding fraction values and mutual information obtained for natural stimulation were much lower than those obtained for artificial stimulation (Wilcoxon rank sum tests; coding fraction: $Z = 7.19$, $P \approx 6.3 \times 10^{-13}$; mutual information: $Z = 5.20$, $P \approx 2.0 \times 10^{-7}$). To establish that our results were not limited to velocity-based representations of self-motion, we repeated our analysis using other representations (e.g., position, acceleration, and jerk). We then computed an optimal kernel that was then convolved with the spike train to obtain the reconstructed stimulus (see Materials and Methods). Overall, the quality of the stimulus reconstruction was poor as quantified by coding fraction values near zero independently of sensory representation (fig. S3). Thus, single vestibular cortical neurons do not transmit information about the detailed time course of natural self-motion.

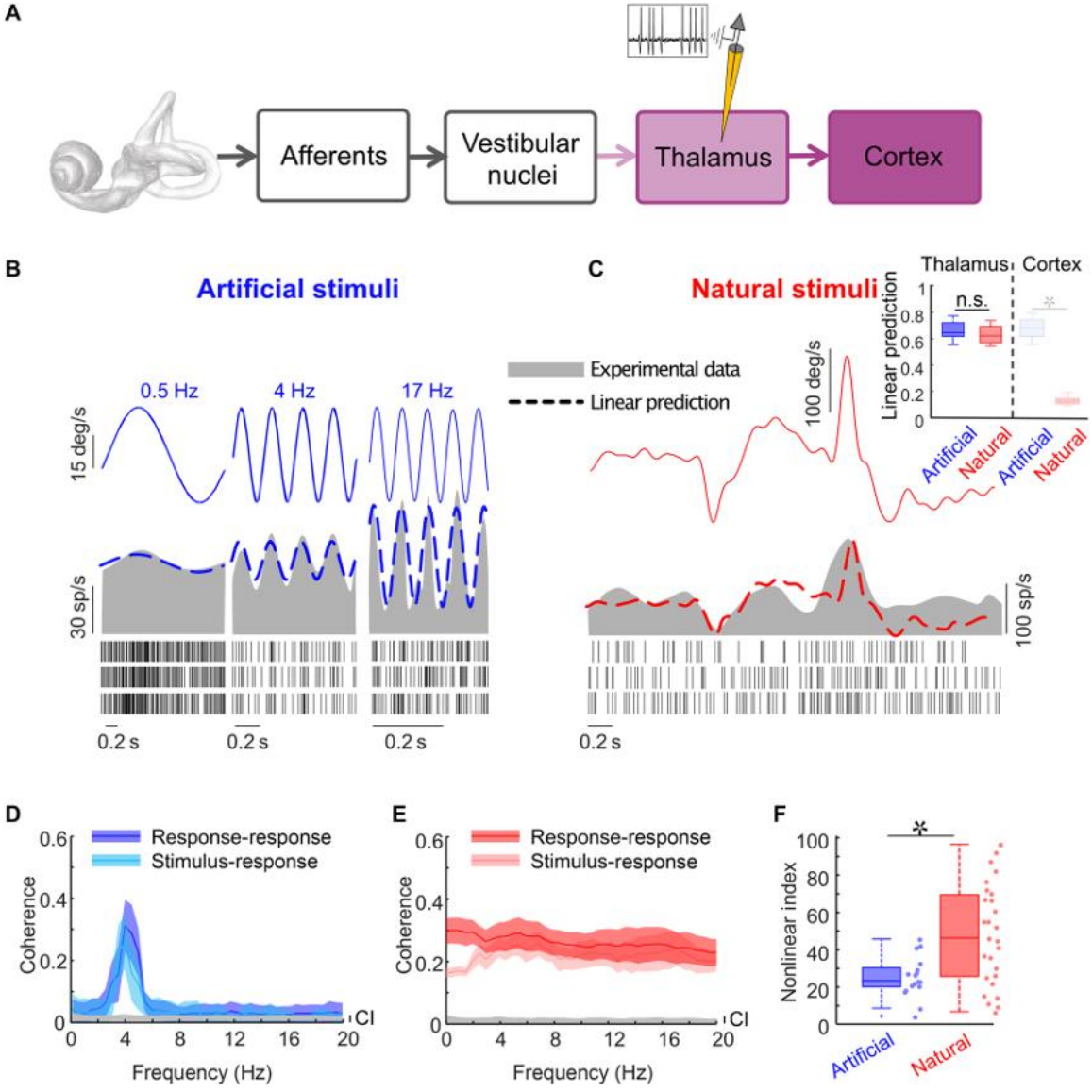

Fig. 3. Vestibular thalamic neurons encode the detailed time course of natural and artificial stimuli. (**A**) Schematic showing ascending vestibular pathways; recordings were made from vestibular thalamic neurons. (**B**) Angular velocity (top), firing rate (middle), and UA (bottom) from an example thalamic neuron during artificial stimulation. Shown are stimulus waveforms (top), firing rates (middle), and UAs (bottom) for three frequencies (left: 0.5 Hz; middle: 4 Hz; right: 17 Hz). The firing rate followed the detailed time course of the stimulus and was well predicted by linear models (dashed line). (**C**) Same as (B), but for natural stimulation. The firing rate followed the detailed time course of the stimulus and was well predicted by linear models (dashed line). Inset: The goodness of fit was not significantly different during both conditions (Wilcoxon signed-rank, $Z = -1.61$, $P \approx 0.11$). Goodness of fit values obtained for thalamic neurons during natural stimulation were significantly higher than those obtained for cortical neurons (Wilcoxon signed-rank, $Z = -7.39$, $P \approx 1.42 \times 10^{-13}$). n.s., not significant. (**D**) Plots showing the population-averaged stimulus-response (light blue) and square root of response-response coherence (dark blue) curves as a function of frequency during artificial 4-Hz sinusoidal stimulation. (**E**) Plots showing the population-averaged stimulus-response (light red) and square root of response-response coherence (dark red) curves as a function of frequency during natural stimulation. (**F**) Whisker-box plots showing the nonlinearity index during artificial (blue) and natural (red) stimulation. Values during natural and artificial stimulation, although significantly different from one another (Wilcoxon signed-rank test, $Z = -2.53$, $P \approx 0.01$), were much more similar than for cortical neurons (compare with Fig. 2F).

In contrast, for thalamic neurons, coding fraction and mutual information values were high during both natural and artificial stimulation, indicating faithful representation of the stimulus' detailed time course in both cases. Coding fraction and mutual information values were significantly higher during natural stimulation (Wilcoxon signed-rank tests; coding fraction: $Z = -4.08$, $P \approx 4.4 \times 10^{-5}$; mutual information: $Z = -4.94$, $P \approx 7.9 \times 10^{-7}$).

PIVC neurons reliably signal the occurrence of specific natural stimulus features via burst firing

Thus far, our results show that vestibular cortical neural activity does not convey information as to the stimulus' detailed time course during natural but not artificial stimulation. This difference is not simply inherited from thalamic afferent input. We therefore next investigated whether specific spike patterns carried information about the

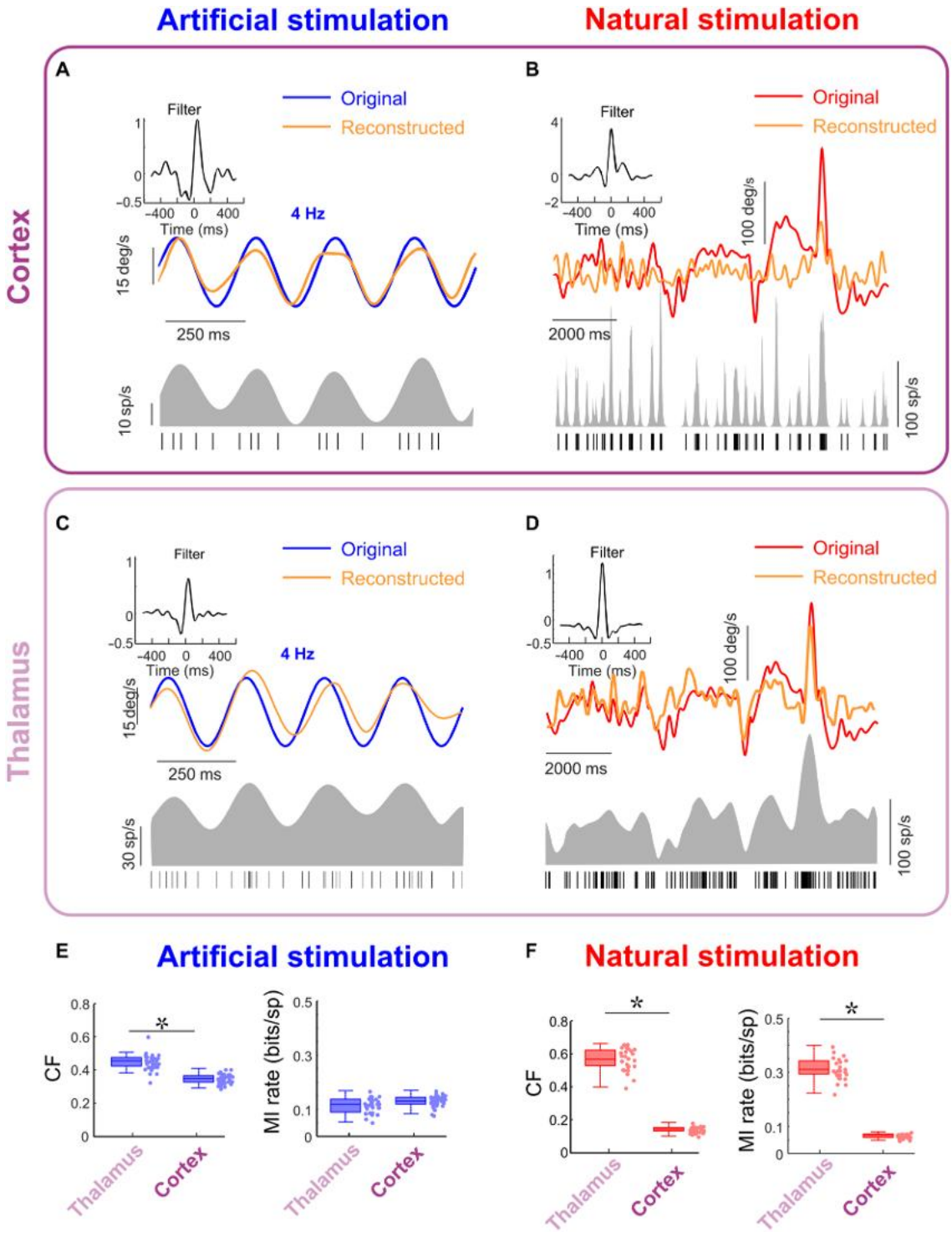

Fig. 4. An optimal linear decoder can recover information as to the stimulus' detailed time course from the spiking activities of vestibular thalamic but not cortical neurons during natural stimulation. (**A**) Top: Original (blue) and reconstructed (orange) stimulus waveforms from an example cortical neuron during artificial stimulation. Bottom: Time-dependent firing rate and UA. Inset: Optimal filter that, when convolved with the UA, gives rise to the reconstructed stimulus waveform. (**B**) Same as (A) and for the same cortical neuron, but during natural stimulation. Note the poor reconstruction. (**C** and **D**) Same as (A) and (B), but for an example thalamic neuron. Note the good quality of the reconstruction in both cases. (**E**) Whisker-box plots for coding fraction (CF) (left) and mutual information (MI) rate (right) for thalamic and cortical neurons during artificial stimulation. The coding fraction was significantly higher for thalamic neurons (Mann-Whitney *U* test, $U = 805$; $P \approx 3.7 \times 10^{-7}$) but not the mutual information rate (Mann-Whitney *U* test, $U = 450$; $P \approx 0.86$). (**F**) Same as (E), but during natural stimulation. Coding fraction and mutual information rate values were significantly higher for thalamic neurons (coding fraction: $U = 875$; $P \approx 5.7 \times 10^{-11}$; mutual information: $U = 875$; $P \approx 6.2 \times 10^{-11}$). "*" indicates statistical significance at the $P < 0.05$ level using a Mann-Whitney *U* test.

stimulus. A closer inspection of spiking responses revealed that vestibular cortical neurons tended to fire clusters of action potentials in response to natural stimulation (Fig. 5A). The interspike interval (ISI) distribution was bimodal with the trough located at 8.0 ms (Hartigan's dip test; dip = 0.09, $P \approx 0.0$; Fig. 5A, right inset), which is a signature of burst firing (*25*). We thus separated the spikes that belong to bursts (i.e., the burst train) from those that did not (i.e., the isolated spike train) using an ISI threshold whose value was set to that corresponding to the trough of the ISI distribution (Fig. 5A, right inset, red arrow; see Materials and Methods). Such methodology has been used in other systems (*44*–*47*). We next examined the relationship between the burst and isolated spike trains and the stimulus. Overall, we found that bursts occurred during specific stimulus features (Fig. 5A, compare green train and dashed black waveform). The stimulus waveforms that triggered bursts all closely resemble one another when *z*-scored as seen from large overlap when superimposed (Fig. 5A, middle right inset). In contrast, isolated spikes were triggered by a wide variety of stimulus waveforms that did not overlap when superimposed (Fig. 5A, bottom right inset). Feature detection via burst firing was not observed during artificial stimulation as the stimulus segments preceding bursts did not overlap (Fig. 5B).

We next used signal detection theory (*48*) to quantify the efficacy of bursts at detecting specific stimulus features (*44*, *47*) (Fig. 6A; see Materials and Methods). Specifically, the distribution of stimulus waveforms within a time window of 30 ms corresponding to the integration timescale for neurons within ascending vestibular pathways (*18*) that preceded either burst spikes, all spikes, or isolated spikes were compared to those that preceded the absence of spiking and the separability between these were assessed by computing the receiver operating characteristic (ROC) curve. The ROC is a plot of the probability of correct detection as a function of the probability of false alarm and quantifies the performance of an ideal observer at correctly deciding which distribution a given sample is coming from. If performing at chance level, then the probability of correct detection is equal to the probability of false alarm (Fig. 6A, right, dashed blue line). In contrast, for perfect performance, the probability of correct detection is equal to 1 whereas the probability of false alarm is equal to zero.

Figure 6 (B and C) shows the ROC curves obtained from bursts (green), isolated spikes (gray), and the full spike train (black) for an example vestibular cortical neuron during natural and artificial stimulation, respectively. Overall, during natural stimulation, the ROC curve for bursts was always above those of the full spike train and isolated spikes (Fig. 6B). In contrast, during artificial stimulation, all three curves overlapped (Fig. 6C). We quantified results by computing the area under the ROC curve (AUC). Overall, AUC values were significantly higher for bursts during natural stimulation than during artificial stimulation (Mann-Whitney *U* test; $U = 1053$; $P = 2.4 \times 10^{-7}$), as well as those obtained for the full spike train or isolated spikes (Kruskal-Wallis test; $H = 72.8$; $P = 1.6 \times 10^{-16}$; Fig. 6D) across all sinusoidal stimulation frequencies (fig. S2). In particular, all PIVC neurons that met our isolation criterion displayed burst firing and increased feature detection via burst firing during natural stimulation (Fig. 6D). It is important to note that differences between AUC values for bursts during natural and artificial stimulation were not due to differences in stimulus amplitude. Restricting the analysis to low-amplitude segments of the natural stimulus gave similar results (fig. S3). Significantly higher AUC values were obtained for bursts across a wide range of time window values (fig. S4).

We next performed a similar analysis for vestibular thalamic neurons. Because the ISI distributions were not bimodal (fig. S5), we used the same burst threshold values as for vestibular cortical neurons, thereby considering "burst trains" with similar ISI values as for vestibular cortical neurons. Overall, the performance of bursts, the full spike train, and isolated spikes were all similar to one another and close to chance level during either of natural or artificial stimulation (Fig. 6, E to G). Last, comparison of performance at feature detection and information transmission revealed a trade-off between both quantities when comparing cortical and thalamic neurons during natural stimulation but not artificial stimulation (fig. S6). We conclude that vestibular cortical neurons reliably signal the occurrence of specific stimulus features via burst firing during natural but not artificial stimulation and that this property is not inherited from vestibular thalamic neurons that instead transmit information about the stimulus' detailed time course during both conditions.

Feature detection via burst firing emerges under complex stimulus statistics

To gain understanding as to how reliable feature detection by burst firing in vestibular cortical neurons emerges, we built a mathematical model based on the Hodgkin-Huxley formalism and analyzed the model's spiking output in the same way as our experimental data (fig. S7A; see Materials and Methods). Overall, AUC and coding fraction values for the model closely matched experimental observations for the burst, full spike train, and isolated spike train during natural stimulation and artificial stimulation (fig. S7, B and C). Because our analysis strongly suggests that these cannot be explained by differences in stimulus amplitude (fig. S2), we instead focused on the fact that natural but not artificial stimuli contain a spectrum of frequencies and are thus more complex (Fig. 6H). We first used a methodology that allowed us to transition between artificial and natural stimuli. Specifically, we expanded the natural stimulus into a Fourier series (see Materials and Methods). Complexity was quantified using the sample entropy (*49*) (see Materials and Methods). We found that, as we included more terms in the Fourier series, thereby making the resulting stimulus waveform more complex and more similar to that of the natural stimulus, reliability of feature detection by bursts as quantified by the AUC increased (Fig. 6I). Stimuli with complexity as low as 40% that of natural stimuli gave rise to reliable feature detection irrespective of amplitude (Fig. 6I). Next, we tested whether artificial stimuli with sufficient complexity could give rise to reliable feature detection. To do this, we progressively added more sinewaves with different amplitudes and frequencies (see Materials and Methods). Overall, we found that such stimuli also gave rise to reliable feature detection by bursts provided that complexity was sufficiently high (Fig. 6J). Thus, our modeling results show that differences in feature detection are associated with natural stimuli being more complex than artificial stimuli. They show that feature detection by bursts emerges for stimuli containing multiple temporal frequencies (i.e., are sufficiently complex).

PIVC neurons form a distributed representation of natural stimuli

Our results show that single PIVC neurons do not provide reliable information as to the detailed time course of natural stimuli (Fig. 2). However, further analysis revealed that individual neurons reliably signal the occurrence of specific stimulus features via burst firing

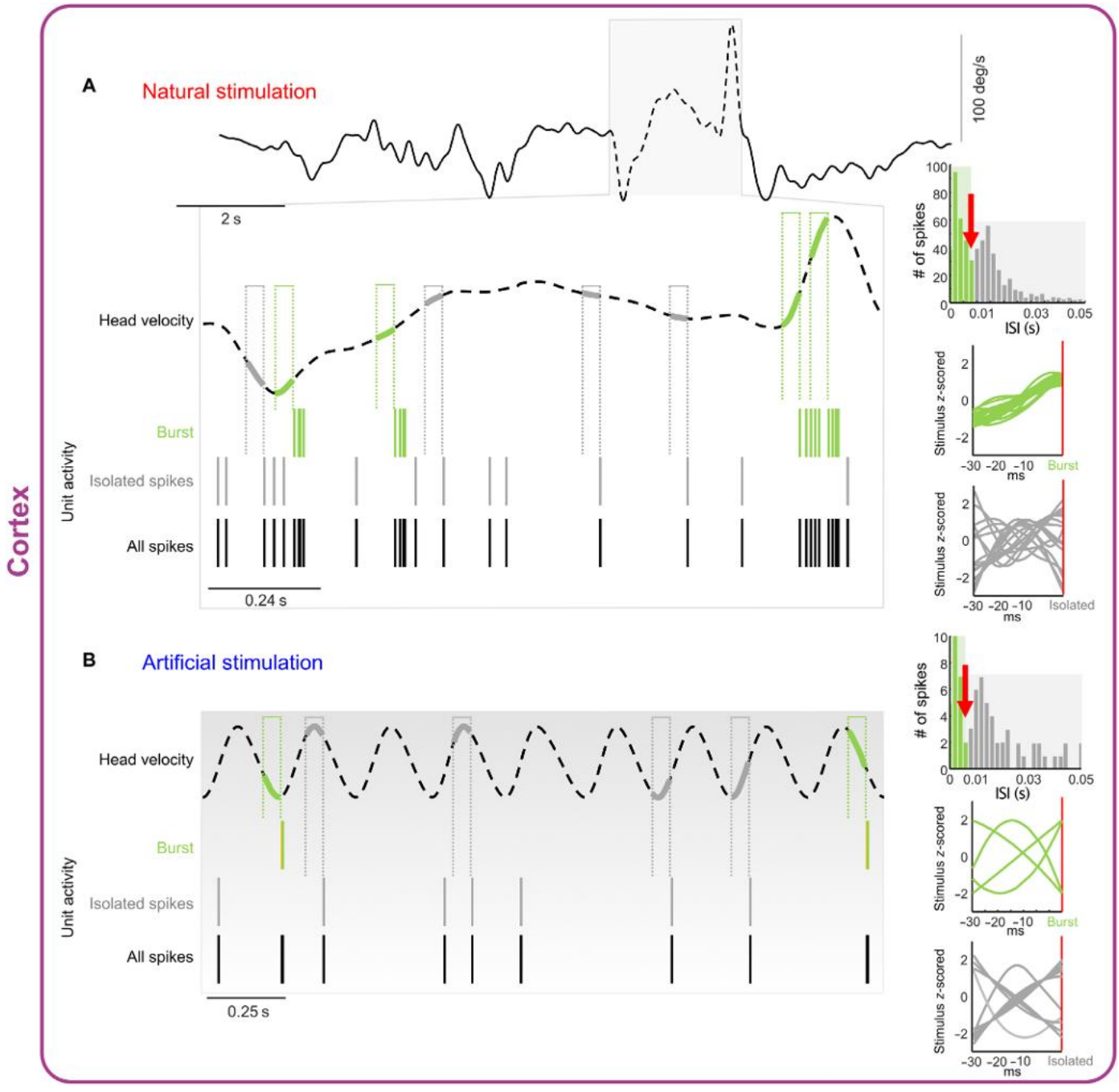

Fig. 5. Vestibular cortical neurons reliably signal the occurrence of specific natural stimulus features through burst firing. (**A**) Natural stimulus waveform (top) with a portion shown in dashed line. The portion of the stimulus waveform (dashed) is shown along with the spiking activity of an example cortical neuron (bottom; black). The ISI distribution from this same neuron was clearly bimodal (top right; Hartigan's dip test; dip statistic: 0.09; $P \approx 0.0$). As such, an ISI threshold (red arrow) of 8.04 ms was used to separate the spikes as those belonging to bursts (green) and isolated spikes (gray). It is seen that bursts always occurred after stimulus upstrokes with varying slope (green portions of the stimulus) that were well aligned with each other (middle right), whereas this was not the case for isolated spikes (gray portions of the stimulus and bottom-right panel). (**B**) Same as (A) and for the same example cortical neuron, but during artificial 4-Hz stimulation. Note that the stimulus waveforms preceding both bursts and isolated spikes were not well aligned with one another in both cases.

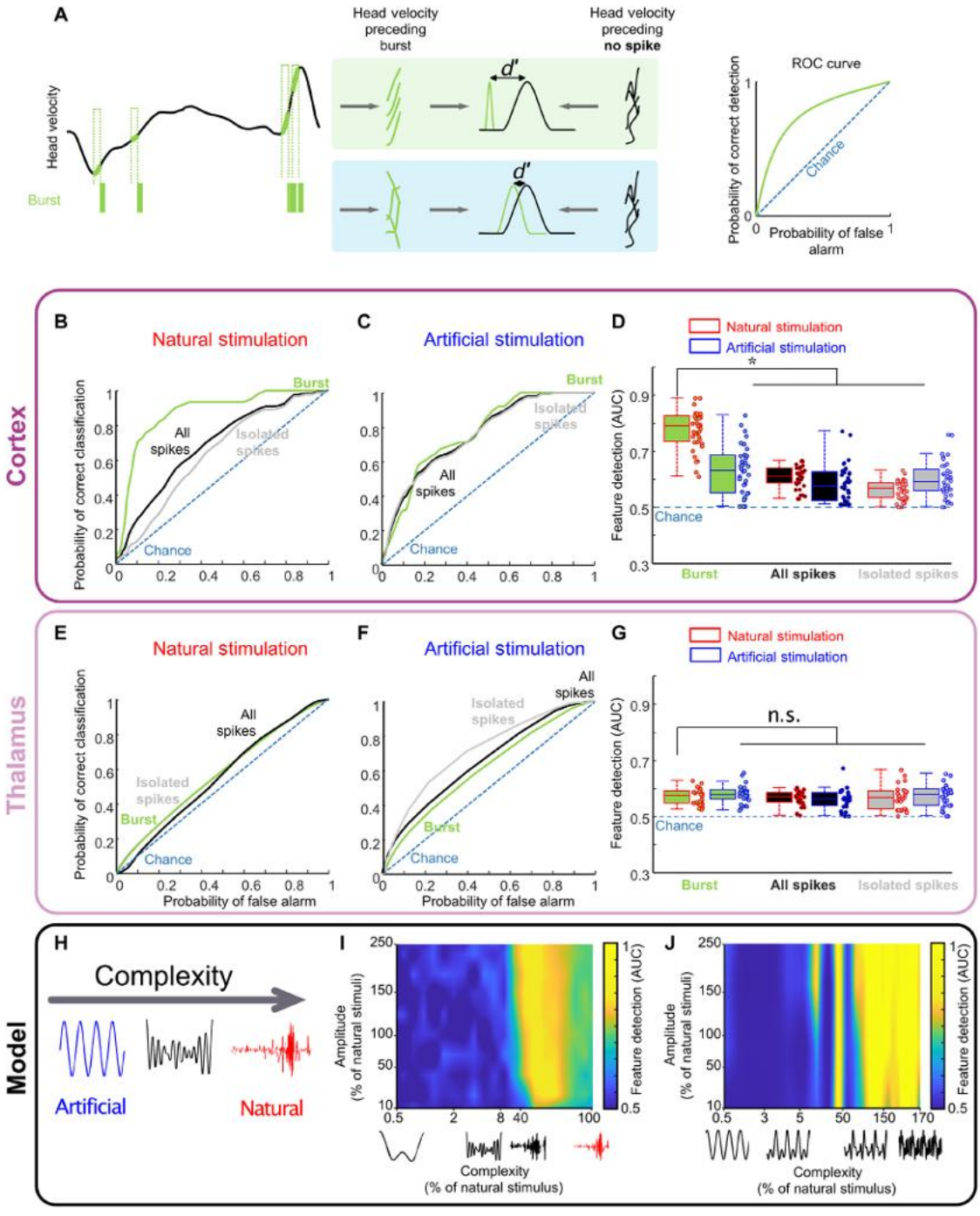

Fig. 6. Vestibular cortical but not thalamic neurons reliably signal the occurrence of stimulus features through burst firing during natural but not artificial stimulation. (**A**) Schematic showing how feature detection was quantified using the bursts as an example. Left: Stimulus waveform (black), burst spike train (green), and stimulus waveforms preceding each burst (i.e., "triggered vectors"; green). Middle: Stimulus waveforms preceding each burst (green) and those preceding the absence of spiking (black). If the stimulus waveforms preceding the bursts are well aligned, the distributions will be more separable (top) than when they are not (bottom). Right: ROC curve (green) and that obtained from chance (dashed blue). (**B**) ROC curves obtained for the burst (green), UA ("all spikes"; black), and isolated (gray) spike trains. Data were pooled from cortical neurons during natural stimulation. (**C**) Same as (B), but during artificial stimulation. (**D**) Whisker-box plots showing the AUC for all spikes (left), isolated spikes (middle), and bursts (right) during natural (red) and artificial (blue) stimulation. AUC values for bursts were significantly higher (Kruskal-Wallis test $H = 72.8$; $P \approx 1.6 \times 10^{-16}$). (**E** and **F**) Same as (B) and (C) (respectively), but for thalamic neurons. (**G**) Same as (D), but for thalamic neurons. AUC values were close to chance and not significantly different (Kruskal-Wallis test $H = 7.11$; $P = 0.21$). (**H**) Stimulus waveforms showing that natural stimuli are more complex than artificial stimuli. (**I**) Color plots showing AUC values obtained from our model when varying both stimulus amplitude (*y* axis) and complexity (*x* axis). (**J**) Same as (I), except that complexity was increased by adding sinusoids with different frequencies and amplitudes, which resulted in stimulus waveforms that were complex but did not resemble the natural stimulus waveform. "*" indicates statistical significance at the $P < 0.05$ level using a Kruskal-Wallis test.

(Fig. 5). Although burst firing from a single neuron by itself is not sufficient to transmit information as to the stimulus' detailed time course, it is conceivable that pooling the burst spike trains of multiple PIVC neurons could provide such information, but only if different neurons were to signal different stimulus features. To test whether this hypothesis is viable, we first constructed a population of model PIVC neurons that each signaled the occurrence of different stimulus features via burst firing (Fig. 7A) before experimental validation. We found that, when summing the burst spike trains of only six neurons to obtain the network activity, burst firing occurred on most of the stimulus waveform (Fig. 7A, bottom). We quantified the ability of an optimal linear decoder at reconstructing the stimulus' detailed time course from the burst spike trains using the stimulus reconstruction technique (Fig. 7B). Each neuron's activity was convolved with a kernel before being summed to obtain the reconstructed stimulus (see Materials and Methods). As for single neurons, the kernels are chosen such as to minimize the mean square error between the actual and reconstructed stimulus waveforms. We found that pooling the activities of vestibular cortical neural populations allowed for accurate reconstruction of the natural stimulus waveform (Fig. 7C) as quantified by the coding fraction which increased with population size (Fig. 7D).

We tested modeling predictions by performing the same analysis on experimental data. Experimental data revealed that different PIVC neurons reliably signaled the occurrence of different stimulus features via burst firing (Fig. 8A), such that burst firing occurred during most of the stimulus waveform when considering only six neurons (Fig. 8A, bottom). We next used the stimulus reconstruction technique but assigned different filters to the different neurons (Fig. 7B). Increasing population size gave rise to improved coding fraction (Fig. 8B, left) and mutual information (Fig. 8B, right). Specifically, pooling the activities of 30 vestibular cortical neurons gave rise to accurate stimulus reconstruction (Fig. 8B, left, inset). In contrast, the activities of thalamic neurons were much more similar to one another (fig. S8A). Pooling the activities of vestibular thalamic neurons did not lead to as great of a relative improvement as cortex when considering either coding fraction or mutual information (Fig. 8, B to D, and fig. S8B). We quantified spike train similarity by computing pairwise correlation coefficient between the responses of different neurons. Overall, the correlation coefficient distribution for cortex had a lower median and was significantly different than that for thalamus (Kolmogorov-Smirnov test; Kolmogorov-Smirnov = 0.32; $P = 4.9 \times 10^{-23}$; Fig. 8C). We also computed the redundancy (see Materials and Methods) and found significantly greater values for vestibular thalamic neurons (Mann-Whitney U test; $U = 0$; $p = 5.7 \times 10^{-11}$; Fig. 8D, right). Thus, our results demonstrate that nonlinear coding via distributed burst firing in the vestibular cortex optimizes coding by reducing redundancy.

Crucially, such differences were not found during artificial stimulation, as the activities of vestibular cortical and thalamic neural populations more closely resembled one another (fig. S9, A to C). As such, the absolute pairwise correlation coefficient between vestibular cortical and thalamic neurons was significantly higher during artificial stimulation ($P \approx 1.14 \times 10^{-78}$; fig. S10). Moreover, plots of the coding fraction and mutual information as a function of population size closely overlapped one another for both areas (fig. S9D). The implications of our results are summarized and discussed below.

DISCUSSION

Summary of results

Our findings reveal a fundamental transformation of vestibular processing between the thalamus and the cortex. Although both vestibular thalamic and cortical neurons encoded the detailed time course of artificial sinusoidal motion, consistent with earlier reports, cortical responses diverged notably from their thalamic inputs during naturalistic self-motion: Whereas thalamic neurons continued to encode the overall dynamics of the stimulus through graded firing rate modulations, cortical neurons instead used a qualitatively distinct coding strategy. Further analysis revealed burst firing that was reliably triggered by specific stimulus features of natural motion, such as stimulus upstrokes. In contrast, isolated spikes—or even the full spike train considered as a whole—failed to show the same level of feature detection. For artificial stimulation, bursts, isolated spikes, and the full spike trains all exhibited comparatively weak coding, underscoring the selectivity and specificity of burst-based coding for natural stimuli. A simple model of burst generation reproduced these experimental results, showing that reliable feature detection by bursts emerges when stimulus statistics are sufficient complex by containing multiple frequencies. Together, these results establish a previously unrecognized cortical computation for vestibular signals: PIVC transforms thalamic input into a distributed, population code optimized for detecting specific features of natural self-motion (e.g., upstrokes) by reducing redundancy. As detailed below, we hypothesize that this representation is a signature of nonlinear mixed selectivity, which further optimizes decoding by downstream areas during multisensory integration. Overall, our results argue that a critical rethinking of how self-motion perception arises during natural behaviors is necessary.

A distributed representation of natural self-motion stimuli by burst firing in the vestibular cortex: implications for other systems

To our knowledge, all previous investigations of neural responses within the vestibular cortex have considered all action potentials collectively and therefore did not focus on specific action potential patterns such as bursts (*9*, *10*, *13*, *34*, *50*). Here, we demonstrated that taking burst firing into account revealed a fundamental property of vestibular cortical neurons, namely, their ability to reliably signal specific stimulus features. Burst firing is a commonly encountered action potential pattern observed across systems (e.g., visual, auditory, somatosensory, and electrosensory), brain regions ranging from sensory areas to hippocampus as well as the avian forebrain, and species ranging from insects to mammals (*26*–*30*) [for review see (*25*, *31*, *32*, *51*–*53*)] and is thought to serve multiple functions at the single-neuron level such as enhancing the signal-to-noise ratio (*54*, *55*), signaling the low-frequency components of time-varying stimuli (*45*, *56*), as well as the detection of specific stimulus features (*44*, *47*) such as contrast (*57*). More recent studies have instead focused on neural populations and shown that burst firing can generate invariant representations of behaviorally relevant stimuli (*58*) as well as more reliable feature detection through increased synchronization (*57*, *59*–*61*).

In contrast, natural stimuli were represented by vestibular cortical neurons in a fundamentally different manner, such that burst firing was elicited by different stimulus features and thus became more dissimilar across neurons, allowing for reduced redundancy and generating a distributed stimulus representation. This latter finding is consistent with recent studies showing that the temporal order of

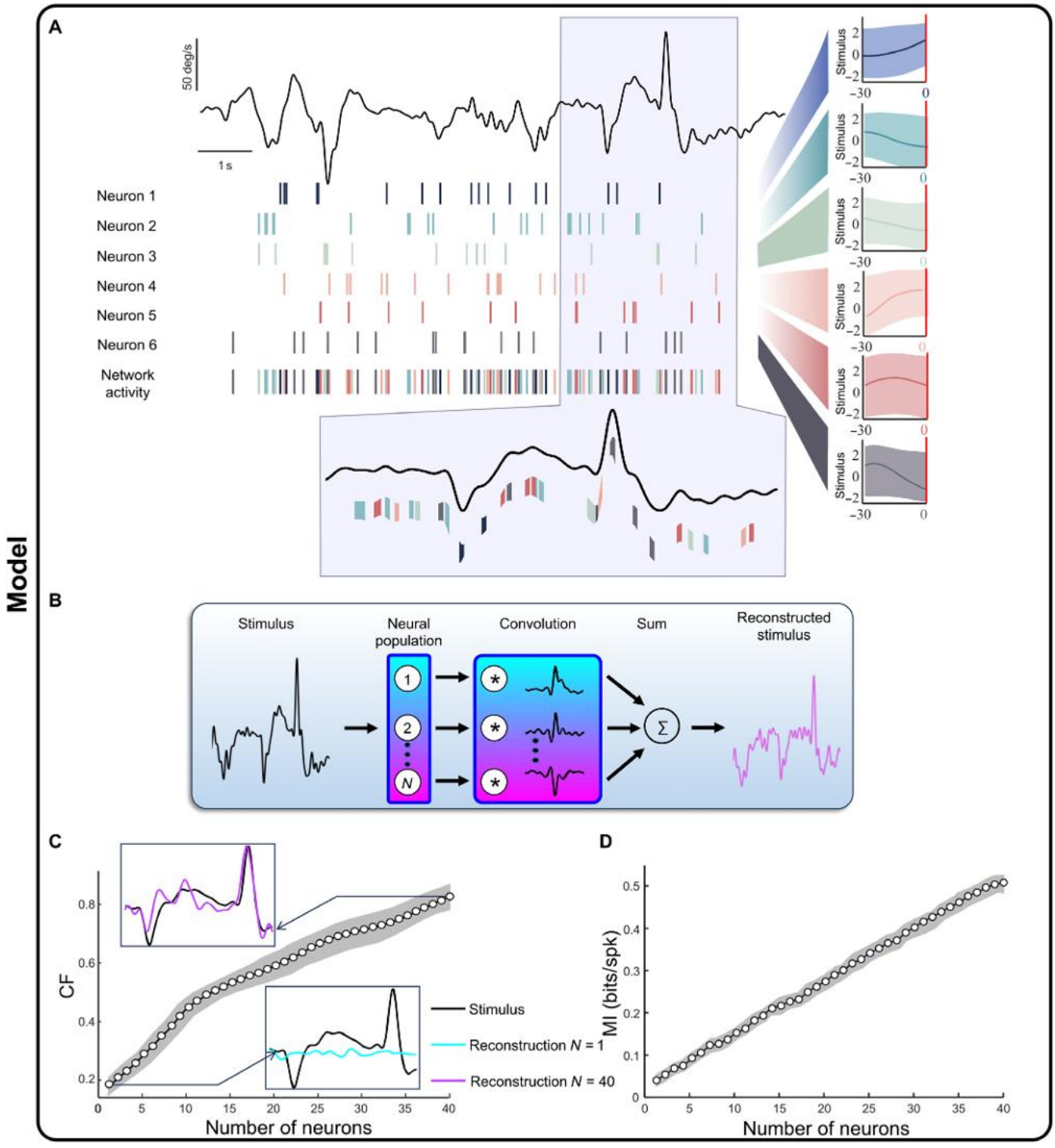

Fig. 7. A simple biophysical model of burst firing reproduces experimental data and predicts a distributed representation of natural self-motion stimuli by vestibular cortical neurons. (**A**) Natural stimulus waveform (top), burst spike trains from six different vestibular cortical neurons (middle), and burst network activity (i.e., sum of burst spike trains). Each neuron reliably signaled the occurrence of different stimulus features through burst firing (right). The bottom panel shows a zoom in of the stimulus waveform (black) and shows the occurrence of the bursts from the different neurons through different colors. It is seen that the bursts from just these six neurons "cover" a large portion of the stimulus waveform already. (**B**) Schematic showing how the stimulus (left) gives rise to spiking activity for multiple neurons (middle left) that are each convolved with separate kernels and summed (middle right) to generate the reconstructed stimulus (right). The kernels are chosen such as to minimize the mean square error between the actual and reconstructed stimulus waveforms. (**C**) Coding fraction as a function of the number of model neurons during natural stimulation. The insets show the original (black) and reconstructed (cyan and magenta) for $N = 1$ (bottom left) and $N = 30$ (top right) neurons. (**D**) Mutual information rate as a function of the number of model neurons during natural stimulation.

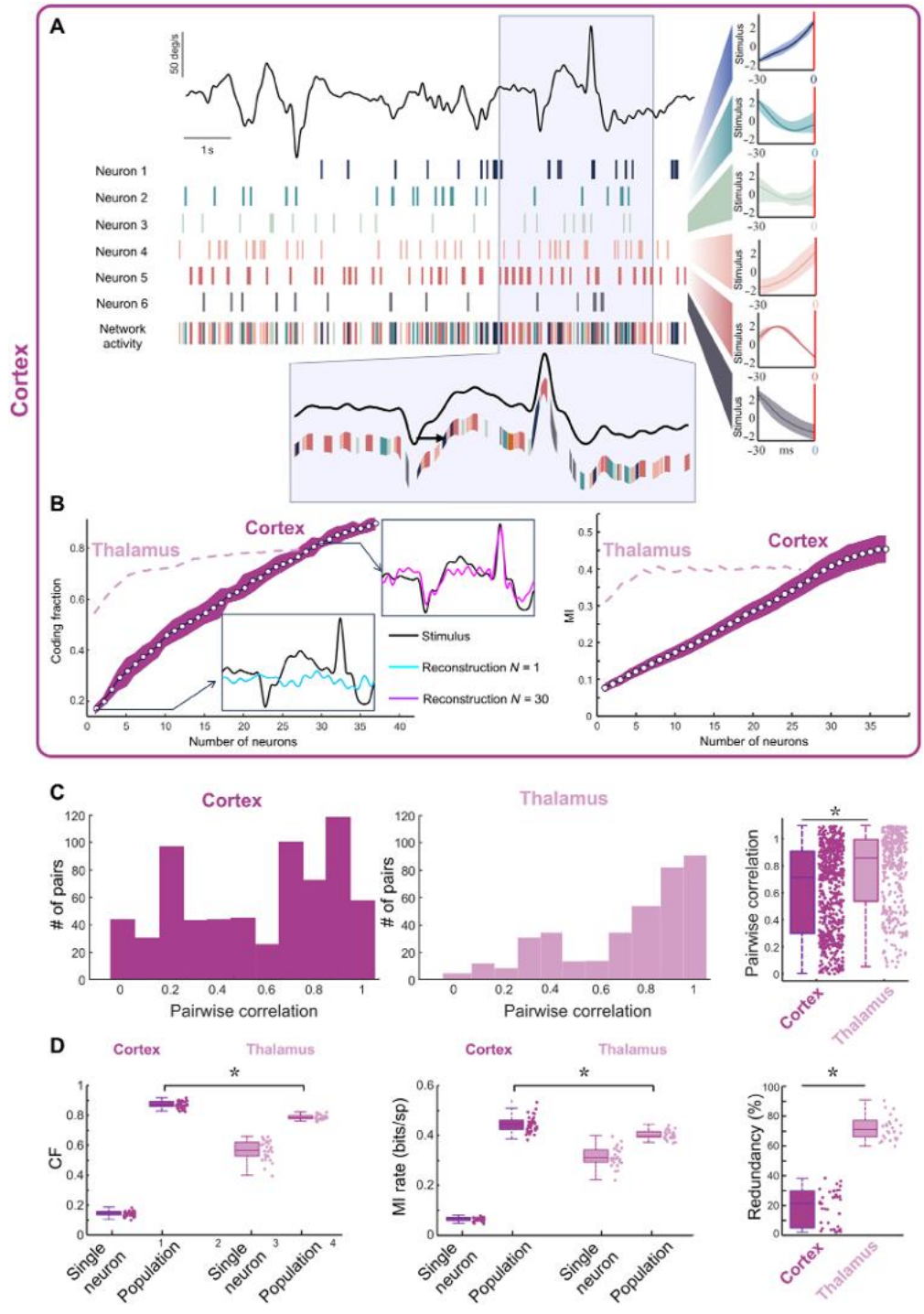

Fig. 8. Vestibular cortical neural populations carry information about the detailed time course of natural stimuli. (**A**) Natural stimulus waveform (top), burst spike trains from experimental data obtained from six different vestibular cortical neurons (middle), and burst network activity (i.e., sum of burst spike trains). Each neuron reliably signaled the occurrence of different stimulus features through burst firing (right). The bottom panel shows a zoom in of the stimulus waveform (black) and shows the occurrence of the bursts from the different neurons through different colors. It is seen that the bursts from just these six neurons "cover" a large portion of the stimulus waveform already. (**B**) Coding fraction (left) and mutual information rate (right) as a function of the number of neurons during natural stimulation. The insets show the original (black) and reconstructed (cyan and magenta) for $n = 1$ (bottom left) and $n = 37$ (top right) neurons. The dashed lines show the same quantities but for thalamic neurons. (**C**) Distribution of pairwise correlation coefficients between neural activities for cortical (left) and thalamic (middle) neurons. Both distributions were significantly different from one another as seen from the Whisker-box plot (right; Wilcoxon signed-rank test, $Z = -8.06$, $P \approx 7.84 \times 10^{-16}$). (**D**) Whisker-box plots showing coding fraction (left) and mutual information rate (middle) values for single neurons and populations. Whisker-box plot showing redundancy (right) for cortical and thalamic neurons (Mann-Whitney U test, $U = 0$; $P = 5.7 \times 10^{-11}$).

burst firing within cortical neural populations can carry information about the stimulus that is distinct from that carried via firing rate or spike latency during more complex natural visual stimulation (*51*, *62*, *63*). As such, the differential coding of artificial versus natural stimuli dependent on complexity uncovered in the present study is likely to generalize across systems. Further studies comparing neural population responses to natural and artificial stimuli are, however, needed to verify this prediction. It is moreover likely that our results will also generalize to other functions of burst firing beyond sensory processing. Within the hippocampus, burst firing has been proposed to increase information transmission via increased synaptic efficacy (*27*, *64*). Within the avian forebrain, burst firing can also help strengthen the vocal output through better coordination of neural activities via plasticity (*65*, *66*). Further studies should investigate how burst firing can enable distributed coding within neural populations in these areas.

What are the mechanisms enabling reliable detection by bursts of specific stimulus features in vestibular cortical populations during natural but not artificial stimulation? Our experimental results show that burst firing is not induced during natural stimulation as it is present during artificial stimulation also. Our modeling results rather show that such feature detection is present when stimulus statistics are sufficiently complex. Thus, rather than requiring an explicit switching mechanism, burst-based feature encoding likely emerges naturally from the nonlinear dynamics of cortical neurons when driven by inputs with richer temporal structure. Further studies are needed to better understand the mechanisms mediating the switch from faithful encoding during artificial to reliable feature detection by burst firing during natural stimulation in vestibular cortical neurons.

Coding of natural self-motion stimuli in the vestibular cortex: implications for multisensory integration and self-motion perception

PIVC is strongly connected to other vestibular areas, the primary and secondary somatosensory cortices, and the premotor and posterior parietal cortices. It also sends projections to the VN in the brainstem (*67*). In general, it is thought that area PIVC is a multisensory region that integrates vestibular, visual, and somatosensory information to create a representation of head-in-space motion that is used to control eye movements, posture, and balance (*68*). This area is thus thought to play an important role in bodily awareness and cognition (*12*, *34*, *69*). Previous results have shown that stimulation of this area in patients produces vestibular sensations (*11*), whereas lesions impair orientation perception (*12*) and increase psychophysical detection thresholds (*13*) [see (*1*) for review].

Our results reveal that vestibular cortical neurons use very different strategies to represent natural versus artificial self-motion stimuli. Although subcortical areas such as the VN (*18*, *19*) and thalamus (*20*) also display differential coding, there are important differences with the cortex. Subcortical vestibular brain areas such as the VN are optimized to encode natural self-motion based on their statistics, and such optimized coding is further refined at the level of the thalamus, thereby allowing single neurons to transmit detailed information as to stimulus' detailed time course to cortical areas by increasing information transmission (*20*). Vestibular thalamic neurons in our dataset responded to artificial stimuli in a manner similar to that reported previously (*38*, *39*), suggesting that the observed responses accurately represent the input to the vestibular cortex. Despite receiving information as to the stimulus' detailed time course, our results show that single cortical neurons do not transmit this information independently of sensory representation but rather reliably signal the presence of distinct stimulus features (e.g., upstrokes), such that it is necessary to pool neural activities to recover information as to the natural self-motion stimulus' detailed time course. As such, our results demonstrate that optimization occurs at the population rather than the single-neuron level within the vestibular cortex.

What advantage does representing natural self-motion stimuli through distributed burst feature coding within the vestibular cortex provide? To address this question, it is important to consider that natural stimuli are inherently more complex than the artificial stimuli commonly used in sensory testing across modalities [visual: (*70*); auditory: (*71*); somatosensory: (*72*); vestibular: (*15*); electrosensory: (*73*)]. Context plays an essential role in interpreting such complex stimuli; the presence or absence of a specific feature often depends on the presence or absence of other contextual features (*74*). We propose that distributed coding via burst firing in the vestibular cortex enables efficient detection and encoding of behaviorally relevant stimulus features embedded within the complex, multidimensional self-motion patterns experienced during everyday life.

In addition, it is useful to remember that self-motion perception is achieved by integration of multiple senses including vestibular, visual, and proprioceptive (*1*, *75*). Vestibular inputs and visual optic flow signals are the two most important cues for perceiving self-motion (*75*). However, visual self-motion cues are not encoded by subcortical vestibular brain areas (*68*). Rather, multisensory integration occurs within the vestibular cortex. Area PIVC is the site of a rich multisensory convergence of vestibular and visual cues during self-motion (*9*, *10*, *76*). The observed distributed coding via burst firing observed here is consistent with vestibular cortical neurons within PIVC neurons using nonlinear mixed selectivity (i.e., a neural code for which neurons respond nonlinearly to a combination of random stimulus features across modalities) to represent natural vestibular and visual self-motion cues. Nonlinear mixed selectivity has been observed across sensory cortices (*77*–*79*) and is thought to be advantageous by providing a solution to the problem as to how reliable perception and behavior can be achieved using unreliable neurons displaying high trial-to-trial variability (*80*). Further studies using combined natural vestibular and visual input are needed to test these predictions. Such studies should also investigate how information from cortical area PIVC is decoded by higher order areas such as the VIP. Specifically, we predict that decoding by VIP will be more optimal during natural than during artificial stimulation.

In this context, our results showing differential coding of natural versus artificial self-motion within the vestibular cortex have important consequences for understanding the function of area PIVC in self-motion processing for perception. This is because we found that vestibular cortical neurons do not merely relaying vestibular information to higher-order cortical areas but instead actively transform incoming natural vestibular input. Thus, a comprehensive rethinking of how self-motion is represented within the brain to mediate perception is likely necessary as natural self-motion stimuli are processed in a fundamentally different manner than the artificial stimuli that have been used to date.

MATERIALS AND METHODS

Ethics statement

All procedures including surgeries, experiments, and housing of the animals were approved by the McGill University Animal Care

Committee (protocol #4096) and in accordance with the guidelines of the Canadian Council on Animal Care.

Surgical procedure

Aseptic surgeries in preparation for extracellular recording and eye movement measurement were performed as described previously (*19*, *20*, *42*). Briefly, one male and two female rhesus monkeys (*M. mulatta*) were preanesthetized with ketamine hydrochloride (15 mg/kg intramuscular) and injected with buprenorphine (0.01 mg/kg im) and diazepam (1 mg/kg im) to provide analgesia and muscle relaxation, respectively. Loading doses of dexamethasone (1 mg/kg im) and cefazolin (50 mg/kg intravenously) were administered to minimize swelling and prevent infection, respectively. Anticholinergic glycopyrrolate (0.005 mg/kg im) was also preoperatively injected to stabilize heart rate and to reduce salivation and then every 2.5 to 3 hours during surgery. During surgery, anesthesia was maintained using isoflurane gas (0.8 to 1.5%), combined with a minimum of 3 liters/min (dose adjusted to effect) of 100% oxygen.

Heart rate, blood pressure, respiration, and body temperature were monitored throughout the procedure. The aseptic magnetic resonance imaging (MRI)–guided surgical techniques has been described previously (*20*). Briefly, the animals were implanted with a custom-made medical grade titanium head post for restraining the head and a recording chamber that was placed on the basis of the coregistration of a Computed Tomography (CT) scan, an MRI scan, and the rhesus brain atlas in Brainsight (Brainsight 2 Vet, Rogue Research, Montreal, Canada) to provide access to PIVC. PIVC access position was confirmed postsurgery by the coregistration of a second CT scan with a recording electrode maintained in the center of the recording chamber. The implant was chronically fastened to the skull with titanium screws and Simplex P bone cement (Stryker Orthopedics, Mahwah, NJ). Craniotomy was performed within the recording chamber to allow electrode access to the brainstem. An 18-mm-diameter eye coil (three loops of Teflon-coated stainless steel wire) was implanted in one eye behind the conjunctiva (*81*). Following surgery, we continued dexamethasone (0.5 mg/kg im; for 4 days), anafen (2 mg/kg day 1, 1 mg/kg on subsequent days), and buprenorphine (0.01 mg/kg im; every 12 hours for 2 to 5 days). In addition, cefazolin (25 mg/kg) was injected twice daily for 10 days. Animals recovered in 2 weeks before any experimenting began.

Data acquisition

During the experiment, animals were head fixed and seated comfortably on a primate chair mounted on a motion platform that delivered head motion stimuli during passive whole-body rotation (pWBR) (*21*). For electrophysiological recordings, a neural probe (NeuroNexus Vector Array, Ann Arbor, MI) with 32 recording sites was used to collect extracellular recording data from multiple individual neurons at a time (shank thickness: 75 μm; area of each recording site: 177 μm^2; vertical distance between sites: 50 μm; horizontal distance between sites: 43.3 μm). The probe was inserted in a guide tube and directed toward the PIVC. The angular velocity and gaze position signals were measured using a gyroscope and a magnetic search coil, respectively, and the signals were low-pass filtered at 125 Hz and sampled at 1000 Hz. Extracellular recording data were band-pass filtered at 300 to 3000 Hz, sampled at 30 kHz, and collected via a Cerebus Neural Signal Processor (BlackRock Systems).

Experimental paradigm

The PIVC was localized by coregistering an MRI with two CT scans: one obtained before surgery and the other afterward. Isolated cells were tested for vestibular sensitivity and lack of eye movement sensitivity by training the animals to perform smooth pursuit, saccades, and vestibulo-ocular reflex (VOR) cancellation (VORc) before the recordings. Specifically, a fixed target was displayed at the center of a screen in front of the animal. After the fixation period, saccadic eye movements were elicited via the presentation of a target at positions ±10°, ±20°, and ±30°. Smooth pursuit movements were elicited by moving a target sinusoidally on the screen with a span of ±30°. Each recorded neuron's firing rate was then quantified for different eye positions as done previously and only neurons for which there was no significant correlation between firing rate and eye position were retained (*21*). The monkeys performed VOR by fixating on a fixed target at the center of the screen during 0.5-Hz sinusoidal pWBR. Moreover, the animals performed VORc during 0.5-Hz pWBR while fixating on a target on the screen which moved synchronously with the primate chair and animal. Upon confirming stable isolation and the absence of eye movement modulation in the PIVC neuron, recordings were initiated as outlined below.

Area VPL of the thalamus was located relative to the lateral geniculate nucleus, which was recognizable due to the presence of individual neurons that responded to either the onset or offset of a light flashed while lowering the electrode during early recordings (*82*). Each neuron included in the present report demonstrated robust firing rate modulation during sinusoidal, whole-body rotations, and no gain to eye movements during saccades or smooth pursuit (*40*, *83*). Furthermore, we ensured that neurons did not respond to visual stimulation caused by small spots of light presented in the visual field (*82*), as done previously (*20*, *42*, *84*).

Stimulus protocol

Following the characterization of the neurons, an interval of 20 s was used to record the resting discharge activity of the neurons. Next, sinusoidal stimuli with maximum angular velocities of 15°/s and frequencies of 0.5, 1, 2, 3, 4, 5, 8, and 17 Hz were delivered to the animal. Each stimulus was presented for a minimum of 10 cycles (i.e., trials). Neural responses to sinusoidal were used for characterization of PIVC neurons as well as the study of population coding during artificial self-motion. Furthermore, at least four repetitions (i.e., trials) of natural stimuli each lasting 60 s with a maximum head velocity of 200°/s and maximum acceleration of 14700°/s^2 in each direction were delivered. Specifically, the motion platform produced rotations such that the head angular velocity stimulus recorded by a gyroscope mounted on the animal's head matched those experienced during natural activities (e.g., foraging, walking, grooming, and running) (*15*, *16*, *18*, *19*, *21*).

We note that the maximum amplitude of the natural stimulus was higher than that of the artificial sinusoidal stimuli irrespective of frequency. However, the actual amplitude of each frequency component of the natural self-motion stimulus was lower than that of the artificial sinusoids (i.e., 15°/s; Fig. 1C).

Spike sorting

All of the data presented in this paper consisted of well-isolated single units that were recorded on nonoverlapping sites of the probe. As such, unit activities were sorted using MATLAB custom-made

codes as previously done for single-neuron recording (*19*, *20*). Specifically, we used voltage amplitude thresholding and visual inspection to detect the spiking activity from the background noise activity as described previously (*21*). Thus, all neurons that met our isolation criteria and whose isolation could be maintained during stimulation were included in the analysis. We note that studying vestibular processing requires maintaining isolation while physically moving the animal. This is particularly difficult during the vigorous high-amplitude natural self-motion used in the current study.

Data analysis

Data were imported into MATLAB (MathWorks, Natick, MA) programming environment for analysis. Binary sequences of unit activities were generated by setting the sequences at a given time to 1 if a spike happened at that time and to 0, otherwise, and sampled at 1000 Hz using custom-written codes for replaying neuronal recordings and sorting action potentials. The head position signal was calculated by integrating the head velocity signal (*21*). The eye position signal was computed as the difference between gaze and head position signals. The firing rate of the neurons was estimated by applying an optimal low-pass Kaiser filter to unit activities (*85*). A neuron was categorized as a vestibular-only neuron if its response to pWBR stimulus did not depend on the eye movement (saccade as well as smooth pursuit) and if the response to VOR and VORc were identical.

Each neuron was also characterized as either type I or type II if it displayed increased firing rate in response to head movements toward the ipsilateral or contralateral sides, respectively. In practice, this was quantified by computing the phase between the firing rate and a sinusoidal head velocity stimulus at 1 Hz (see below). Neurons whose phases were near 0 were classified as type I whereas neurons whose phases were near 180° were classified as type II.

For sinusoidal stimuli, the firing rate was aligned to be in phase with the head velocity stimulus by computing the cross-correlation and finding the position of the peak, as done previously (*20*). The phase was then obtained from this lag. The gain was computed from the slope of the best-fit straight line when plotting the firing rate aligned with the head velocity stimulus. For naturalistic stimuli, the gain and phase were computed from the cross-spectrum between the head velocity and the firing rate divided by the stimulus power spectrum, as done previously (*19*, *20*). The computed values of gain and phase were then used to build linear models that were used to predict the firing rate. The predicted firing rate was then compared to the experimentally obtained (i.e., actual) firing rate by computing the variance accounted for (VAF) as done previously (*20*).

Stimulus estimation

An estimate of the time-varying stimulus $S(t)$ was obtained from the activities of N neurons by convolving each spike train $R_i(t)$ with a linear filter $K_i(t)$ and adding the contributions of all cells (*43*, *86*)

$$S_{\text{est}}(t) = \sum_{i=1}^{N} \int d\tau\, K_i(\tau) R_i(t-\tau)$$

The filters $K_i(t)$ are chosen to minimize the mean square error ε^2 between the stimulus and its estimate

$$\varepsilon^2 = \left\langle \left[S(t) - S_{\text{est}}(t) \right]^2 \right\rangle$$

where $< \ldots >$ denotes the average over time.

The optimal set of filters are given by (*43*, *86*)

$$\begin{pmatrix} P_{R1R1}(f) & \cdots & P_{RNRn}(f) \\ \vdots & \ddots & \vdots \\ P_{RNR1}(f) & \cdots & P_{RNRN}(f) \end{pmatrix} \begin{pmatrix} \tilde{K}_1(f) \\ \vdots \\ \tilde{K}_N(f) \end{pmatrix} = \begin{pmatrix} P_{SR1}(-f) \\ \vdots \\ P_{SRN}(-f) \end{pmatrix}$$

where $\tilde{K}_i(f)$ is the Fourier transform of $K_i(t)$, $P_{RiRj}(f)$ is the cross-spectrum between $R_i(t)$ and $R_j(t)$, and $P_{SRi}(-f)$ is the cross-spectrum between $S(t)$ and $R_i(t)$. The quality of the reconstruction was assessed by computing the coding fraction (cf), which represents the fraction of the stimulus that is correctly reconstructed (*44*)

$$\text{cf} = 1 - \frac{\varepsilon}{\sigma_{\text{stim}}}$$

where σ_{stim} is the SD of the stimulus $S(t)$. The mutual information (MI) rate was then obtained from

$$\text{MI} = \int_0^{20} df \log_2 \left[\frac{P_{\text{SS}}(f)}{P_{\text{noise}}(f)} \right]$$

where $P_{\text{SS}}(f)$ is the stimulus power spectrum and $P_{\text{noise}}(f)$ is the power spectrum of noise $(t) = S(t) - S_{\text{est}}(t)$. The mutual information rate was normalized by the average firing rate of the neural population. The redundancy was computed as

$$\text{Redundancy} = 100 \times \left(1 - \frac{\text{MI}_N}{\sum_{i=1}^{N} \text{MI}_{1,i}} \right)$$

where MI_N is the mutual information rate computed from a population of N neurons and $\text{MI}_{1,i}$ is the mutual information for single neuron i within that population. Essentially, if the N neurons transmit information independently, then the redundancy is 0%, as expected. In contrast, if all neurons are the same, then the redundancy tends toward 100% as the population size N increases.

Stimulus-response response, response-response coherence, and nonlinearity index

The stimulus-response coherence was computed as (*43*)

$$C_{\text{rs}}(f) = \frac{|P_{\text{SR}}(f)|^2}{P_{\text{RR}}(f) P_{\text{SS}}(f)}$$

where $P_{\text{RR}}(f)$ and $P_{\text{SS}}(f)$ are the response and stimulus power spectra, respectively. The stimulus-response coherence is a measure of linear correlation between the stimulus and neural response and is thus limited both by response trial-to-trial variability and by response nonlinearity (*35*, *36*). The impact of response nonlinearity can be assessed by comparing the stimulus response coherence to the square root of the response-response coherence, which was computed using (*24*)

$$\sqrt{C_{\text{rr}}(f)} = \frac{\sqrt{\frac{2}{k(k-1)} \left| \sum_{i=2}^{k} \sum_{j=1}^{i-1} P_{R_i R_j}(f) \right|^2}}{P_{\text{RR}}(f)}$$

where k is the number of trials (i.e., stimulus repetitions) and R_i and R_j are the responses of a given neuron during trials i and j, respectively. Note that the response-response coherence is only limited by response trial-to-trial variability. Moreover, we always have $C_{rs}(f) \leq \sqrt{C_{rr}(f)}$ for any frequency f with equality only when the response is linearly related to the stimulus. Thus, any difference between the stimulus-response coherence and the square-rooted response-response coherence must be due to nonlinearities (*37*, *87*). The nonlinearity index (NI) was computed as (*24*, *88*)

$$\mathrm{NI} = 100 \times \left[1 - \frac{\int df\, C_{rs}(f)}{\int df \sqrt{C_{rr}(f)}} \right]$$

where the interval of integration was either [0 20] for natural stimulation or within an interval of 2 Hz centered on the stimulus frequency for artificial stimulation. Thus, if the response is linearly related to the stimulus, we have $C_{rs}(f) = \sqrt{C_{rr}(f)}$ and thus NI = 0%. In contrast, in the case where the relationship between stimulus and response is very nonlinear such that the stimulus-response coherence is zero, we then have NI = 100%.

Sensory representations

Sensory representations of the head velocity stimulus were obtained by applying a fractional differentiation operator $\frac{d^\alpha}{dt^\alpha}$ to the head velocity time-varying waveform (*20*, *89*). Here, α is the order and ranges between −1 (position) and 2 (jerk). We note that negative values of α correspond to integration. In the frequency domain, fractional differentiation of order α corresponds to filtering by a transfer function $H_\alpha(f)$ given by (*90*)

$$H_\alpha(f) = (2\pi f)^\alpha \exp\left(\frac{i\alpha\pi}{2}\right)$$

where $i = \sqrt{-1}$.

Burst extraction

We used an ISI threshold representing the average burst threshold across neurons in our datasets to assign each spike as part of a burst or not (i.e. "isolated") and thus generated the burst spike trains and the complementary isolated spike trains (*45*–*47*, *58*, *91*–*93*). Specifically, spikes with an ISI lower or equal than the threshold were assigned as part of a burst with the process continuing until an ISI is greater than the threshold. Spikes that were not part of bursts were deemed to be isolated. The burst fraction was defined as the fraction of ISIs that are less than or equal to a given threshold value. The ISI threshold was chosen to be at the trough separating the two modes of the ISI distribution (Fig. 4B, red arrow) and ranged between 4.3 and 12.1 ms.

Burst feature classification

We quantified the performance of bursts, isolated spikes, and the full spike train at detecting their preferred stimulus feature (*47*). First, the preferred features were computed by accumulating the stimulus waveforms (i.e., the "feature vectors") that preceded each isolated spike (i.e., "isolated"), the first spike of each burst (i.e., "burst"), each action potential in the full spike train (i.e., "spike"), and the lack of action potential firing (i.e., "0") by 30 ms in the main figures. The length of this time window was also systematically varied (fig. S3). The stimulus waveform was sampled at 1 ms. Thus, the set of stimulus waveforms preceding each event (i.e., the "triggered vector") is given by

$$\mathbf{TV_x} = \left[S\left(t_i^x - 0.1\right) \ldots S\left(t_i^x\right) \right]_{i=1}^{N_x}$$

where x = "isolated," "burst," "spike," or "0," and "N_x" denotes the number of features. We note that each vector has 30 elements. We shall denote by "$\overrightarrow{\mathbf{m_x}}$" the mean triggered vector and by "$\mathbf{\Sigma_x}$" the covariance matrices. The optimal feature vectors that maximize the discriminability between the isolated spike, burst, or spike triggered vectors and the "no spike" vectors are given by (*47*)

$$\overrightarrow{\mathbf{FV_x}} = \sum_{i=1}^{n_x} \frac{\nu_i^x}{\lambda_i^x} \overrightarrow{\mathbf{e_i^x}}$$

where λ_i^x and $\overrightarrow{e_i^x}$ are the ith eigenvalue and eigenvector of the matrix $\left(\Sigma_0 + \mathbf{\Sigma_x}\right)/2$, respectively, and $\nu_i^x = \left(\overrightarrow{\mathbf{m_x}} - \overrightarrow{\mathrm{m}_0}\right) \cdot \overrightarrow{\mathbf{e_i^x}}$ with "·" representing the dot product. Note that the eigenvalues are sorted in descending order (i.e., $\lambda_1^x \geq \lambda_2^x \geq \ \ldots \ \geq \lambda_{100}^x \geq 0$). Here, n_x is the smallest integer such that

$$\frac{\sum_{i=1}^{n_x} \lambda_i^x}{\sum_{i=1}^{100} \lambda_i^x} \geq 0.99$$

The sets of projections of the optimal feature vector $\overrightarrow{\mathbf{FV_x}}$ on the triggered vectors were then computed as $\overrightarrow{\mathbf{FV_x}} \cdot \mathbf{TV_x}$. Histograms with 70 bins ranging from the minimum to the maximum value were then used to compute the relevant probability distributions. We compared probability distributions obtained for "isolated," "burst," or "spike" to those obtained in the absence of activity (i.e., "0"). We then used signal detection theory to compute the probability of correct detection P_D and the probability of false alarm P_{FA} by systematically varying a threshold (*48*). The ROC curve was then obtained by plotting P_D as a function P_{FA}. Last, the performance was quantified as the AUC of the ROC curve showing P_D as a function of P_{FA}.

Stimulus complexity and Fourier series

To transition between sinusoidal and natural stimuli, we decomposed the natural stimulus waveform into a Fourier series

$$S(t) = a_0 + \sum_{i=1}^{\infty} \sqrt{a_i^2 + b_i^2} \cos\left[2\pi \frac{i}{T} t - \arctan\left(\frac{b_i}{a_i}\right) \right]$$

where T is the length of the stimulus $S(t)$and

$$a_i = \frac{2}{T} \int_0^T dt\, S(t) \cos\left(2\pi \frac{i}{T} t\right)$$

$$b_i = \frac{2}{T} \int_0^T dt\, S(t) \sin\left(2\pi \frac{i}{T} t\right)$$

we then considered stimulus waveforms $S_N(t)$ given by

$$S_N(t) = a_0 + \sum_{i=1}^{N} \sqrt{a_i^2 + b_i^2} \cos\left[2\pi \frac{i}{T} t - \arctan\left(\frac{b_i}{a_i}\right) \right]$$

As N increases, the waveform $S_N(t)$ will converge toward $S(t)$ such that

$$\lim_{N\to\infty} S_N(t) = S(t)$$

We also considered other artificial waveforms $S_{\text{artificial},M}(t)$, with $M = 1\ldots250$ given by

$$S_{\text{artificial},M}(t) = \sum_{i=1}^{M} \exp\left(-\frac{i}{3760}\right)\sin\left(2\pi\frac{i}{3760}t+\phi_i\right)$$

where the $\{\phi_i\}_{i=1}^{250}$ are drawn independently and randomly from a uniform distribution between $-\pi$ and π. This allowed us to create stimuli whose waveforms did not resemble that of the natural stimulus but with increasing complexity as M increases. In all cases, stimulus complexity was determined by computing the transfer entropy (*49*) using the function "PE.m" in MATLAB.

Mathematical model

We used a biophysically based mathematical model of burst firing based on the Hodgkin-Huxley formalism (*33*). The model consists of two compartments and is based on the Hodgkin-Huxley formalism. The equations describing the membrane voltages in the somatic (V_S) and dendritic (V_D) compartments are given by

$$C_m\frac{dV_S}{dt} = I_{app} + \text{Stimulus}(t) + \varepsilon(t) - I_{Na,S} - I_{K,S} - \frac{g_c}{\kappa}\left(V_S - V_D\right) - I_{leak,S}$$

$$C_m\frac{dV_D}{dt} = -I_{Na,D} - I_{K,D} - \frac{g_c}{1-\kappa}\left(V_D - V_S\right) - I_{leak,D}$$

where $C_m = 1\ \mu\text{F/cm}^2$ is the membrane capacitance, $I_{Na,i}$ and $I_{K,i}$ are the fast inward Na^+ and the slow outward delayed rectifier K^+ currents in the soma ($i = S$) and the dendrite ($i = D$), respectively, I_{app} is the depolarizing current to the somatic compartment, I_{syn} is the synaptic current to the dendritic compartment, and $I_{leak,S}$ and $I_{leak,D}$ are the passive leak currents present in both compartments. Here, Stimulus(t) is the stimulus and $\varepsilon(t)$ is Gaussian white noise with mean 0 and SD σ. In practice, we used either of sinusoidal stimuli, the natural stimulus waveform, as well as the waveforms $S_N(t)$ and $S_{\text{artificial},M}(t)$ as input to the model. The two compartments are linked together through a resistor, where $g_c = 1\ \mu\text{S/cm}^2$ is the maximum conductance and $\kappa = 0.4$ is the somatic-to-dendritic area ratio. The kinetics of the ionic currents included in each compartment ($i = S, D$) are given by

$$I_{Na,S} = g_{Na,S}m_{\infty,S}^2\left(1-n_S\right)\left(V_S - V_{Na}\right)$$

$$I_{K,S} = g_{K,S}n_S^2\left(V_S - V_K\right)$$

$$I_{leak,S} = g_{leak}\left(V_S - V_{leak}\right)$$

$$I_{Na,D} = g_{Na,D}m_{\infty,D}^2h_D\left(V_D - V_{Na}\right)$$

$$I_{K,D} = g_{K,D}n_D^2p_D\left(V_D - V_K\right)$$

$$I_{leak,D} = g_{leak}\left(V_D - V_{leak}\right)$$

where $g_{j,i}$ (j = Na, K, leak, and i = S, D) are the maximum conductances, and V_j (j = Na, K, leak) are the Nernst potentials. Each channel is governed by inactivation and/or activation dynamical gating variables x ($x = n_i, h_D, p_D; i = S, D$) whose steady states and time constants are denoted by x_∞ and τ_x, respectively, and whose dynamics are governed by the equation

$$\frac{dx}{dt} = \frac{x_\infty - x}{\tau_x}$$

The steady state activation/inactivation functions are given by

$$x_\infty\left(V_i\right) = \frac{1}{1+\exp\left[\frac{-\left(V_i - V_{x_i}\right)}{s_{x_i}}\right]},\ x_i = m_i, n_i, h, p;\ i = S, D$$

The parameter values used were (voltages are in mV, current density is in $\mu\text{A/cm}^2$, conductances are in $\mu\text{S/cm}^2$, and time constants are in ms) as follows: $I_{app} = 2$, $g_{Na,S} = 55$, $g_{K,S} = 20$, $g_{leak} = 0.18$, $g_{K,D} = 10.5$, $g_{Na,D} = 5$, $V_{Na} = 40$, $V_K = -88.5$, $V_{leak} = -70$, $\tau_{n_S} = 0.39$, $\tau_{h_D} = 1$, $\tau_{n_D} = 0.9$, $\tau_{p_D} = 5$, $V_{m_S} = V_{n_S} = V_{m_D} = V_{n_D} = -40$, $V_{h_D} = -52$, $V_{p_D} = -65$, $s_{m_S} = s_{n_S} = -3$, $s_{m_D} = s_{n_D} = -5$, $s_{h_D} = 5$, and $s_{p_D} = 6$. These values were chosen on the basis of the previous literature to elicit action potential and burst firing at levels comparable to those seen experimentally (*33*). The differential equations were numerically integrated using a Euler-Maruyama algorithm with a time step of 0.0025 ms. The somatic membrane potential time series from the model were thresholded to obtain spike times and then analyzed in the same way as the experimental data.

Supplementary Materials

The PDF file includes:

Figs. S1 to S10

Legend for movie S1

Other Supplementary Material for this manuscript includes the following:

Movie S1

REFERENCES

1. K. E. Cullen, Vestibular processing during natural self-motion: Implications for perception and action. *Nat. Rev. Neurosci.* **20**, 346–363 (2019).
2. V. Marlinski, R. A. McCrea, Self-motion signals in vestibular nuclei neurons projecting to the thalamus in the alert squirrel monkey. *J. Neurophysiol.* **101**, 1730–1741 (2009).
3. H. Meng, P. J. May, J. D. Dickman, D. E. Angelaki, Vestibular signals in primate thalamus: Properties and origins. *J. Neurosci.* **27**, 13590–13602 (2007).
4. M. Dieterich, P. Bartenstein, S. Spiegel, S. Bense, M. Schwaiger, T. Brandt, Thalamic infarctions cause side-specific suppression of vestibular cortex activations. *Brain* **128**, 2052–2067 (2005).
5. R. Matsuzaki, S. Kyuhou, K. Matsuura-Nakao, H. Gemba, Thalamo-cortical projections to the posterior parietal cortex in the monkey. *Neurosci. Lett.* **355**, 113–116 (2004).
6. S. Akbarian, O. J. Grusser, W. O. Guldin, Corticofugal connections between the cerebral cortex and brainstem vestibular nuclei in the macaque monkey. *J. Comp. Neurol.* **339**, 421–437 (1994).
7. C. Lopez, O. Blanke, The thalamocortical vestibular system in animals and humans. *Brain Res. Rev.* **67**, 119–146 (2011).

8. W. O. Guldin, S. Akbarian, O. J. Grusser, Cortico-cortical connections and cytoarchitectonics of the primate vestibular cortex: A study in squirrel monkeys (Saimiri sciureus). *J. Comp. Neurol.* **326**, 375–401 (1992).
9. O. J. Grusser, M. Pause, U. Schreiter, Localization and responses of neurones in the parieto-insular vestibular cortex of awake monkeys (Macaca fascicularis). *J. Physiol.* **430**, 537–557 (1990).
10. O. J. Grusser, M. Pause, U. Schreiter, Vestibular neurones in the parieto-insular cortex of monkeys (Macaca fascicularis): Visual and neck receptor responses. *J. Physiol. (Lond.)* **430**, 559–583 (1990).
11. W. Penfield, Vestibular sensation and the cerebral cortex. *Ann. Otol. Rhinol. Laryngol.* **66**, 691–698 (1957).
12. T. Brandt, M. Dieterich, A. Danek, Vestibular cortex lesions affect the perception of verticality. *Ann. Neurol.* **35**, 403–412 (1994).
13. A. Chen, G. C. DeAngelis, D. E. Angelaki, Macaque parieto-insular vestibular cortex: Responses to self-motion and optic flow. *J. Neurosci.* **30**, 3022–3042 (2010).
14. J. M. Goldberg, V. J. Wilson, K. E. Cullen, D. E. Angelaki, D. M. Broussard, J. Buttner-Ennever, K. Fukushima, L. B. Minor, *The Vestibular System* (Oxford Univ. Press, 2012).
15. J. Carriot, M. Jamali, M. J. Chacron, K. E. Cullen, Statistics of the vestibular input experienced during natural self-motion: Implications for neural processing. *J. Neurosci.* **34**, 8347–8357 (2014).
16. J. Carriot, M. Jamali, M. J. Chacron, K. E. Cullen, The statistics of the vestibular input experienced during natural self-motion differ between rodents and primates. *J. Physiol.* **595**, 2751–2766 (2017).
17. C. Massot, A. D. Schneider, M. J. Chacron, K. E. Cullen, The vestibular system implements a linear-nonlinear transformation in order to encode self-motion. *PLOS Biol.* **10**, e1001365 (2012).
18. D. E. Mitchell, A. Kwan, J. Carriot, M. J. Chacron, K. E. Cullen, Neuronal variability and tuning are balanced to optimize naturalistic self-motion coding in primate vestibular pathways. *Elife* **7**, e43019 (2018).
19. I. Mackrous, J. Carriot, K. E. Cullen, M. J. Chacron, Neural variability determines coding strategies for natural self-motion in macaque monkeys. *Elife* **9**, e57484 (2020).
20. J. Carriot, G. McAllister, H. Hooshangnejad, I. Mackrous, K. E. Cullen, M. J. Chacron, Sensory adaptation mediates efficient and unambiguous encoding of natural stimuli by vestibular thalamocortical pathways. *Nat. Commun.* **13**, 2612 (2022).
21. M. Mohammadi, J. Carriot, I. Mackrous, K. E. Cullen, M. J. Chacron, Neural populations within macaque early vestibular pathways are adapted to encode natural self-motion. *PLOS Biol.* **22**, e3002623 (2024).
22. K. E. Cullen, J. Carriot, M. J. Chacron, "The vestibular thalamus" in *The Cerebral Cortex and Thalamus*, W. M. Usrey, S. M. Sherman, Eds. (Oxford Academic, 2023), pp. 284–296.
23. K. E. Cullen, M. J. Chacron, Neural substrates of perception in the vestibular thalamus during natural self-motion: A review. *Curr. Res. Neurobiol.* **4**, 100073 (2023).
24. M. Jamali, M. J. Chacron, K. E. Cullen, Self-motion evokes precise spike timing in the primate vestibular system. *Nat. Commun.* **7**, 13229 (2016).
25. R. Krahe, F. Gabbiani, Burst firing in sensory systems. *Nat. Rev. Neurosci.* **5**, 13–23 (2004).
26. R. Azouz, M. S. Jensen, Y. Yaari, Ionic basis for spike after-depolarization and burst generation in adult rat hippocampal CA1 pyramidal cells. *J. Physiol.* **492**, 211–223 (1996).
27. S. Raus Balind, A. Mago, M. Ahmadi, N. Kis, Z. Varga-Nemeth, A. Lorincz, J. K. Makara, Diverse synaptic and dendritic mechanisms of complex spike burst generation in hippocampal CA_3 pyramidal cells. *Nat. Commun.* **10**, 1859 (2019).
28. C. Yue, Y. Yaari, KCNQ/M channels control spike afterdepolarization and burst generation in hippocampal neurons. *J. Neurosci.* **24**, 4614–4624 (2004).
29. R. H. Hahnloser, A. A. Kozhevnikov, M. S. Fee, An ultra-sparse code underlies the generation of neural sequences in a songbird. *Nature* **419**, 65–70 (2002).
30. D. Margoliash, E. S. Fortune, Temporal and harmonic combination-sensitive neurons in the zebra finch's HVc. *J. Neurosci.* **12**, 4309–4326 (1992).
31. G. Marsat, G. S. Pollack, Bursting neurons and ultrasound avoidance in crickets. *Front. Neurosci.* **6**, 95 (2012).
32. M. G. Metzen, R. Krahe, M. J. Chacron, Burst firing in the electrosensory system of gymnotiform weakly electric fish: Mechanisms and functional roles. *Front. Comput. Neurosci.* **10**, 81 (2016).
33. B. Doiron, C. Laing, A. Longtin, L. Maler, Ghostbursting: A novel neuronal burst mechanism. *J. Comput. Neurosci.* **12**, 5–25 (2002).
34. M. E. Shinder, S. D. Newlands, Sensory convergence in the parieto-insular vestibular cortex. *J. Neurophysiol.* **111**, 2445–2464 (2014).
35. J. C. Roddey, B. Girish, J. P. Miller, Assessing the performance of neural encoding models in the presence of noise. *J. Comput. Neurosci.* **8**, 95–112 (2000).
36. F. Theunissen, J. C. Roddey, S. Stufflebeam, H. Clague, J. P. Miller, Information theoretic analysis of dynamical encoding by four identified interneurons in the cricket cercal system. *J. Neurophysiol.* **75**, 1345–1364 (1996).
37. C. L. Passaglia, J. B. Troy, Information transmission rates of cat retinal ganglion cells. *J. Neurophysiol.* **91**, 1217–1229 (2004).
38. H. Meng, D. E. Angelaki, Responses of ventral posterior thalamus neurons to three-dimensional vestibular and optic flow stimulation. *J. Neurophysiol.* **103**, 817–826 (2010).
39. L. Deecke, D. W. Schwarz, J. M. Fredrickson, Vestibular responses in the rhesus monkey ventroposterior thalamus. II. Vestibulo-proprioceptive convergence at thalamic neurons. *Exp. Brain Res.* **30**, 219–232 (1977).
40. V. Marlinski, R. A. McCrea, Activity of ventroposterior thalamus neurons during rotation and translation in the horizontal plane in the alert squirrel monkey. *J. Neurophysiol.* **99**, 2533–2545 (2008).
41. V. Marlinski, R. A. McCrea, Coding of self-motion signals in ventro-posterior thalamus neurons in the alert squirrel monkey. *Exp. Brain Res.* **189**, 463–472 (2008).
42. J. Carriot, K. E. Cullen, M. J. Chacron, The neural basis for violations of Weber's law in self-motion perception. *Proc. Natl. Acad. Sci. U.S.A.* **118**, e2025061118 (2021).
43. F. Rieke, D. Warland, R. R. de Ruyter van Steveninck, W. Bialek, *Spikes: Exploring the Neural Code* (MIT, 1996).
44. F. Gabbiani, W. Metzner, R. Wessel, C. Koch, From stimulus encoding to feature extraction in weakly electric fish. *Nature* **384**, 564–567 (1996).
45. A. M. M. Oswald, M. J. Chacron, B. Doiron, J. Bastian, L. Maler, Parallel processing of sensory input by bursts and isolated spikes. *J. Neurosci.* **24**, 4351–4362 (2004).
46. N. A. Lesica, G. B. Stanley, Encoding of natural scene movies by tonic and burst spikes in the lateral geniculate nucleus. *J. Neurosci.* **24**, 10731–10740 (2004).
47. W. Metzner, C. Koch, R. Wessel, F. Gabbiani, Feature extraction by burst-like spike patterns in multiple sensory maps. *J. Neurosci.* **18**, 2283–2300 (1998).
48. D. Green, J. Swets, *Signal Detection Theory and Psychophysics* (John Wiley & Sons, 1966).
49. J. S. Richman, J. R. Moorman, Physiological time-series analysis using approximate entropy and sample entropy. *Am. J. Physiol. Heart Circ. Physiol.* **278**, H2039–H2049 (2000).
50. S. Akbarian, K. Berndl, O. J. Grusser, W. Guldin, M. Pause, U. Schreiter, Responses of single neurons in the parietoinsular vestibular cortex of primates. *Ann. N. Y. Acad. Sci.* **545**, 187–202 (1988).
51. A. Luczak, B. L. McNaughton, K. D. Harris, Packet-based communication in the cortex. *Nat. Rev. Neurosci.* **16**, 745–755 (2015).
52. J. Shao, Y. Liu, D. Gao, J. Tu, F. Yang, Neural burst firing and its roles in mental and neurological disorders. *Front. Cell. Neurosci.* **15**, 741292 (2021).
53. Z. Friedenberger, E. Harkin, K. Toth, R. Naud, Silences, spikes and bursts: Three-part knot of the neural code. *J. Physiol.* **601**, 5165–5193 (2023).
54. A. Kepecs, J. Lisman, Information encoding and computation with spikes and bursts. *Network* **14**, 103–118 (2003).
55. J. E. Lisman, Bursts as a unit of neural information: Making unreliable synapses reliable. *Trends Neurosci.* **20**, 38–43 (1997).
56. O. Avila-Akerberg, M. J. Chacron, In vivo conditions influence the coding of stimulus features by bursts of action potentials. *J. Comput. Neurosci.* **31**, 369–383 (2011).
57. A. N. Sanchez, H. J. Alitto, D. L. Rathbun, T. G. Fisher, W. M. Usrey, Stimulus contrast modulates burst activity in the lateral geniculate nucleus. *Curr. Res. Neurobiol.* **4**, 100096 (2023).
58. M. G. Metzen, A. Akhshi, P. Bashivan, A. Khadra, M. J. Chacron, Burst firing optimizes invariant coding of natural communication signals by electrosensory neural populations. *iScience* **28**, 112399 (2025).
59. T. Womelsdorf, S. Ardid, S. Everling, T. A. Valiante, Burst firing synchronizes prefrontal and anterior cingulate cortex during attentional control. *Curr. Biol.* **24**, 2613–2621 (2014).
60. P. Bonifazi, M. Goldin, M. A. Picardo, I. Jorquera, A. Cattani, G. Bianconi, A. Represa, Y. Ben-Ari, R. Cossart, GABAergic hub neurons orchestrate synchrony in developing hippocampal networks. *Science* **326**, 1419–1424 (2009).
61. A. C. Kwan, Y. Dan, Dissection of cortical microcircuits by single-neuron stimulation in vivo. *Curr. Biol.* **22**, 1459–1467 (2012).
62. N. D. Nguyen, A. Lutas, O. Amsalem, J. Fernando, A. Y. Ahn, R. Hakim, J. Vergara, J. McMahon, J. Dimidschstein, B. L. Sabatini, M. L. Andermann, Cortical reactivations predict future sensory responses. *Nature* **625**, 110–118 (2024).
63. W. Xie, J. H. Wittig Jr., J. I. Chapeton, M. El-Kalliny, S. N. Jackson, S. K. Inati, K. A. Zaghloul, Neuronal sequences in population bursts encode information in human cortex. *Nature* **635**, 935–942 (2024).
64. S. J. Moore, D. C. Cooper, N. Spruston, Plasticity of burst firing induced by synergistic activation of metabotropic glutamate and acetylcholine receptors. *Neuron* **61**, 287–300 (2009).
65. R. H. Hahnloser, C. Z. Wang, A. Nager, K. Naie, Spikes and bursts in two types of thalamic projection neurons differentially shape sleep patterns and auditory responses in a songbird. *J. Neurosci.* **28**, 5040–5052 (2008).
66. S. Moorman, J. R. Ahn, M. H. Kao, Plasticity of stereotyped birdsong driven by chronic manipulation of cortical-basal ganglia activity. *Curr. Biol.* **31**, 2619–2632.e4 (2021).
67. W. O. Guldin, S. Mirring, O. J. Grusser, Connections from the neocortex to the vestibular brain stem nuclei in the common marmoset. *Neuroreport* **5**, 113–116 (1993).
68. K. E. Cullen, The vestibular system: Multimodal integration and encoding of self-motion for motor control. *Trends Neurosci.* **35**, 185–196 (2012).

69. M. Dieterich, T. Brandt, "Chapter 24—Functional brain imaging of the vestibular system: fMRI and PET" in *Handbook of Clinical Neurophysiology* (Elsevier, 2010), vol. 9, pp. 303–312.
70. D. L. Ruderman, W. Bialek, Statistics of natural images: Scaling in the woods. *Phys. Rev. Lett.* **73**, 814–817 (1994).
71. M. S. Lewicki, Efficient coding of natural sounds. *Nat. Neurosci.* **5**, 356–363 (2002).
72. C. P. de Kock, B. Sakmann, Spiking in primary somatosensory cortex during natural whisking in awake head-restrained rats is cell-type specific. *Proc. Natl. Acad. Sci. U.S.A.* **106**, 16446–16450 (2009).
73. C. G. Huang, M. G. Metzen, M. J. Chacron, Descending pathways mediate adaptive optimized coding of natural stimuli in weakly electric fish. *Sci. Adv.* **5**, eaax2211 (2019).
74. M. Banyai, A. Lazar, L. Klein, J. Klon-Lipok, M. Stippinger, W. Singer, G. Orban, Stimulus complexity shapes response correlations in primary visual cortex. *Proc. Natl. Acad. Sci. U.S.A.* **116**, 2723–2732 (2019).
75. D. E. Angelaki, K. E. Cullen, Vestibular system: The many facets of a multimodal sense. *Annu. Rev. Neurosci.* **31**, 125–150 (2008).
76. W. O. Guldin, O. J. Grusser, Is there a vestibular cortex? *Trends Neurosci.* **21**, 254–259 (1998).
77. K. M. Walker, J. K. Bizley, A. J. King, J. W. Schnupp, Multiplexed and robust representations of sound features in auditory cortex. *J. Neurosci.* **31**, 14565–14576 (2011).
78. I. Rentzeperis, A. R. Nikolaev, D. C. Kiper, C. van Leeuwen, Distributed processing of color and form in the visual cortex. *Front. Psychol.* **5**, 932 (2014).
79. A. Finkelstein, N. Ulanovsky, M. Tsodyks, J. Aljadeff, Optimal dynamic coding by mixed-dimensionality neurons in the head-direction system of bats. *Nat. Commun.* **9**, 3590 (2018).
80. S. Fusi, E. K. Miller, M. Rigotti, Why neurons mix: High dimensionality for higher cognition. *Curr. Opin. Neurobiol.* **37**, 66–74 (2016).
81. A. F. Fuchs, D. A. Robinson, A method for measuring horizontal and vertical eye movement chronically in the monkey. *J. Appl. Physiol.* **21**, 1068–1070 (1966).
82. R. T. Marrocco, Sustained and transient cells in monkey lateral geniculate nucleus: Conduction velocities and response properties. *J. Neurophysiol.* **39**, 340–353 (1976).
83. J. E. Roy, K. E. Cullen, Selective processing of vestibular reafference during self-generated head motion. *J. Neurosci.* **21**, 2131–2142 (2001).
84. A. Dale, K. E. Cullen, The ventral posterior lateral thalamus preferentially encodes externally applied versus active movement: Implications for self-motion perception. *Cereb. Cortex* **29**, 305–318 (2019).
85. S. Cherif, K. E. Cullen, H. L. Galiana, An improved method for the estimation of firing rate dynamics using an optimal digital filter. *J. Neurosci. Methods* **173**, 165–181 (2008).
86. C. Massot, M. J. Chacron, K. E. Cullen, Information transmission and detection thresholds in the vestibular nuclei: Single neurons versus population encoding. *J. Neurophysiol.* **105**, 1798–1814 (2011).
87. M. J. Chacron, Nonlinear information processing in a model sensory system. *J. Neurophysiol.* **95**, 2933–2946 (2006).
88. M. Jamali, J. Carriot, M. J. Chacron, K. E. Cullen, Coding strategies in the otolith system differ for translational head motion vs. static orientation relative to gravity. *Elife* **8**, e44573 (2019).
89. I. Podlubny, *Fractional Differential Equations: An Introduction to Fractional Derivatives, Fractional Differential Equations, to Methods of Their Solution and Some of Their Applications* (Academic Press, 1999).
90. C. G. Huang, Z. D. Zhang, M. J. Chacron, Temporal decorrelation by SK channels enables efficient neural coding and perception of natural stimuli. *Nat. Commun.* **7**, 11353 (2016).
91. O. Avila-Akerberg, R. Krahe, M. J. Chacron, Neural heterogeneities and stimulus properties affect burst coding in vivo. *Neuroscience* **168**, 300–313 (2010).
92. N. Khosravi-Hashemi, E. S. Fortune, M. J. Chacron, Coding movement direction by burst firing in electrosensory neurons. *J. Neurophysiol.* **106**, 1954–1968 (2011).
93. M. M. Marquez, M. J. Chacron, Serotonin increases population coding of behaviorally relevant stimuli by enhancing responses of ON but not OFF-type sensory neurons. *Heliyon* **9**, e18315 (2023).

Acknowledgments

Funding: This work was supported by the Canadian Institutes of Health Research (http://cihr-irsc.gc.ca/; funding reference number PJT-203699); received by J.C., K.E.C., and M.J.C.

Author contributions: Conceptualization: J.C., I.M., K.E.C., and M.J.C. Data curation: J.C., I.M., K.E.C., and M.J.C. Formal analysis: J.C., I.M., K.E.C., and M.J.C. Funding acquisition: J.C., K.E.C., and M.J.C. Investigation: J.C., I.M., K.E.C., and M.J.C. Methodology: J.C., I.M., K.E.C., and M.J.C. Project administration: K.E.C. and M.J.C. Resources: J.C. and M.J.C. Software: J.C., I.M., K.E.C., and M.J.C. Supervision: K.E.C. and M.J.C. Validation: J.C., I.M., K.E.C., and M.J.C. Visualization: J.C., I.M., K.E.C., and M.J.C. Writing—original draft: J.C., I.M., K.E.C., and M.J.C. Writing—review and editing: J.C., I.M., K.E.C., and M.J.C. **Competing interests:** The authors declare that they have no competing interests. **Data, code, and materials availability:** All data and code needed to evaluate and reproduce the results in the paper are either present in the paper and/or the Supplementary Materials or are available from the Borealis database (https://borealisdata.ca/privateurl.xhtml?token=37880b0e-d761-4ab3-8ca7-b1371119bfce). This study did not generate new materials.

Submitted 16 December 2025
Accepted 29 June 2026
Published 7 August 2026
10.1126/sciadv.aee8327

Science Advances

Distributed burst firing mediates optimized cortical encoding of natural self-motion

Jerome Carriot, Isabelle Mackrous, Kathleen E. Cullen, and Maurice J. Chacron

Sci. Adv. **12** (32), eaee8327. DOI: 10.1126/sciadv.aee8327

Science Advances (ISSN 2375-2548) is published by the American Association for the Advancement of Science. 1200 New York Avenue NW, Washington, DC 20005. The title *Science Advances* is a registered trademark of AAAS.